Acta Biomaterialia 198 (2025) 334–355

Contents lists available at ScienceDirect

Acta Biomaterialia

journal homepage: www.elsevier.com/locate/actbio

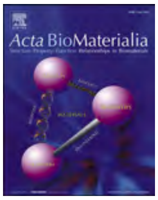

Full length article

Evaluating the single crystallinity of sea urchin calcite

Sebastian Hoerl [a,*], Erika Griesshaber [a], Antonio G. Checa [b], Aimo Winkelmann [c], Frank Förster [a,d], Osama Alsheikha [a,e], Felix Hidalgo [f], Elena Sturm [a], Sandro Jahn [a], Wolfgang W. Schmahl [a]

[a] Department für Geo- und Umweltwissenschaften, Ludwig-Maximilians-Universität München, Munich 80333, Germany
[b] Departamento de Estratigrafía y Paleontología, Universidad de Granada, Granada 18071, Spain
[c] Academic Centre for Materials and Nanotechnology (ACMiN), AGH University of Krakow, Krakow 30-059, Poland
[d] Department of Earth Sciences, University of Geneva, Geneva 1205, Switzerland
[e] Faculty of Biology, Chemistry & Earth Sciences, University of Bayreuth, Bayreuth 95447, Germany
[f] Departamento de Zoología, Universidad de Granada, Granada 18071, Spain

ARTICLE INFO

Keywords:
EBSD
Biomineralisation
Sea urchins
EBSP matching
Microstructure/texture

ABSTRACT

Recent advancements in electron backscatter diffraction (EBSD) data evaluation enable the determination of misorientation between crystals below 0.1°, while with conventional EBSD data evaluation, the smallest misorientation precision between crystals scatters between 0.5°-1°. Sea urchin tests and spines are lightweight biomaterials with a serrated microstructure comprising interlinked calcite crystals. We investigated the microstructure and crystallographic texture of *Cidaris cidaris* and *Paracentrotus lividus* test and spine calcite with advanced EBSD measurement and data evaluation. In particular, we re-evaluated the widely accepted single-crystallinity of sea urchin calcite. We found that the test and the spines comprise calcite crystals with different fabrics and a significant variation in crystal co-orientation strength. Even the highly co-oriented calcite of *C. cidaris* and *P. lividus* is not perfectly single-crystalline. We found test and spine portions that feature significant internal misorientations (1-3°). Test c-axis orientation in *C. cidaris* is tangential to the outer test surface, while in the spines, it is parallel to the morphological axis of the spine. Primary and secondary spines feature a bimodal crystal texture comprising co-oriented calcite surrounded by a cortex of misoriented crystals. Crystal misorientation in the spine cortex seems to result mainly from competitive growth determinants. Deciphering the degree of crystallinity and mode of crystal organisation of biological hard tissues is vital for understanding their exceptional control of structure, material architecture and material properties.

Statement of significance: Echinoids form lightweight biomineralised skeletal elements with outstanding material properties and a complex microstructure formed of interlinked calcite crystals. The degree of crystallinity and the crystallographic organisation of the calcitic tests and spines are still under debate. We investigate and discuss the crystallinity, microstructure, and texture of *Cidaris cidaris* and *Paracentrotus lividus* test and spine crystals. Unprecedented and not yet used for biomineralised carbonate tissues, we apply electron backscatter diffraction pattern matching data evaluation, enabling detection of misorientation precision below 0.1°, relative to 0.5°-1° misorientation precision obtained from conventional EBSD data evaluation. We demonstrate that sea urchin test plates and spines are not single crystals. They feature internal small-angle misorientations and poorly co-oriented, polycrystalline regions with intricate microstructures.

1. Introduction

Echinoids are among the many organisms that secrete Ca-carbonate skeletons, which serve various functions, including locomotion and protecting their soft tissue and major organs from environmental hazards [1,2]. In contrast to molluscs, brachiopods and bryozoans that use an epithelial system for hard tissue mineralisation, echinoderms use a syncytium for mineral formation [3]. The epithelial system of biomineralisation involves the transfer of ions, secretes proteinaceous substances and minerals and generates rather compact layers of a

---

* Corresponding author.
E-mail address: s.hoerl@lmu.de (S. Hoerl).

https://doi.org/10.1016/j.actbio.2025.03.044
Received 2 December 2024; Received in revised form 5 March 2025; Accepted 25 March 2025

composite material, which, in general, consists of a structured biopolymer matrix filled with small-sized crystals [3]. At biomineralisation via syncytia, the cells generate large three-dimensional mineral units with a perforated pattern [3]. Forming sizable skeletal elements of large fenestrated crystals enables the fabrication of structures that are lightweight and, at the same time, rigid and resistant [3,4]. Indeed, many studies demonstrate how echinoderms profit from their lightweight skeletons having exquisite mechanical properties [5–10]. Echinoids form their skeleton and skeletal elements of high-Mg calcite [11]. The calcite comprises the test (composed of many large crystal plates with a stereom architecture), the spines (anchored by muscles entwined around the struts of the test tubercles), the pedicellariae (stalked appendages containing skeletal supports protruding from the surface of the test) and the chewing apparatus (consisting of the jaw bone that surrounds the five teeth). The latter is present in many, but not in all echinoids [11–13]. Nonetheless, even though the test covers the soft tissue of the organism, the echinoid test is regarded to be a mesodermal internal skeleton, with the test encasing the major organs of the animal. The outer surfaces of the test and spines, however, are coated by a thin layer of skin and muscles.

The crystallography of echinoderm calcite crystals is well-investigated by now [14–16]. Each echinoid skeletal element has a specific crystallographic pattern that, in general, is consistent within sea urchin species, genera, families, and even orders [17]. The crystal texture of echinoid tests shows two modes of crystallographic calcite axes orientation: The c-axes are oriented either (1) perpendicular to the test plate surfaces or (2) tangential to the curvature of the test in the aboral direction [18]. In the case of the spines, the orientation of the calcite crystallite c-axes follows the orientation of the morphological long axes of the spines [19].

Nonetheless, even though sea urchin calcite crystal orientation patterns are well determined by now, the crystallinity of the calcite is still controversial and under debate. The question that is not resolved yet is whether the crystals or crystallites of the test and the spines are single crystals, mesocrystals, or even little textured polycrystals. Hence, assessing the degree of misorientation between adjacent crystals/crystallites is of main scientific importance. X-ray diffraction studies of Su et al., Moureaux et al., Nissen and Donnay and Pawson [19–22], and results of the etching protocols of Okazaki et al [23] suggest that sea urchin spines are large single crystals, while the studies of Seto et al [24,25] and Cölfen et al [26] define the calcite of sea urchin spines as meso- or mosaic crystals.

The development of high-resolution crystallographic analysis techniques, particularly electron backscatter diffraction (EBSD), allows us to refine our knowledge of the crystallography of individual crystals obtained from transmission electron microscopy (TEM) imaging and texture determination with X-ray diffraction (XRD) measurements and Rietveld data analysis. In contrast to XRD or TEM, EBSD measurements provide spatially resolved information and have a significantly larger field of view. This renders the EBSD technique as a powerful technique for material science, in particular, for the analysis of structural hard tissues, biologically secreted or man-made. However, a key factor for high-resolution EBSD measurements is its angular precision. The main factors influencing and determining the angular precision of EBSD scans are the method used for identifying and locating the EBSD pattern and the selected pattern indexing technique. With conventional Hough-based indexing techniques, EBSD can perform minimal misorientation determination with an angular orientation precision between 0.5° and 1° [27]. Recently, new approaches to EBSD pattern indexing have been developed, which are based on the direct correlation between experimentally determined and simulated EBSD patterns [28–31]. This results in a marked improvement in angular precision and allows the determination of misorientation between adjacent crystals below 0.1°. Accordingly, the above described advanced EBSD pattern indexing technique (subsequently named EBSD pattern matching) enables the determination of minute misorientations in a crystalline material. Sea urchin calcite is ideal for investigating misorientations and, particularly, minute misorientations in a structural material, as it was, up to now, often regarded to be a single-crystalline biomaterial [16,32].

In this study, we investigate in great detail the test and spine calcite of the sea urchin *Cidaris cidaris* (Linnaeus, 1758). We complement our results with measurements gained on the test and spine of *Paracentrotus lividus* (Lamarck, 1816). The class Echinoidea consists of two sub-classes, Perischoechinoidea and Euechinoidea. For comparative reasons, we chose to investigate the calcite of a species belonging to Perischoechinoidea (*C. cidaris*) and of a species belonging to the Euechinoidea (*P. lividus*). Both species live in comparable marine environments, in waters of the eastern Atlantic and of the Mediterranean Sea [33], are epibenthic and dwell on all types of surfaces of the shelf region [34,35]. While *P. lividus* inhabits shallower and more highly energetic habitats, *C. cidaris* is mostly found in quieter environments and deeper waters [36,37]. For protection and locomotion, *C. cidaris* uses its test but also its long and, from each other, widely separated primary and the smaller, on the test densely distributed, secondary spines [2]. In *C. cidaris*, each interambulacral plate features one primary spine. The latter is surrounded by multiple secondary spines which protect the primary muscle attachment zones together with the pedicellariae [36,38,39]. For *P. lividus,* the protective test is very densely covered with the long and sharply pointed primary spines as well as with the small secondary spines. This study is part of a larger project aiming to understand the microstructure and crystallographic texture of echinoid skeletal elements, investigating, in particular, the nature of the misorientations between the calcite crystallites [40].

Using high-resolution EBSD for our microstructural analysis, we report both EBSD measurements and maps evaluated with conventional and electron backscatter pattern matching modes. First, we give an overview of the crystallographic architecture of the test, the tubercles as well as the primary and secondary spines. We highlight the misorientations found in the above-mentioned sea urchin skeletal elements. These were, previously, reported to be single-crystalline [16]. We show the misorientation angle distribution gained from conventional EBSD data evaluation as well as refined by the EBSD pattern matching method and highlight the range of misorientations in the calcite of the investigated sea urchin species. For *P. lividus* and *C. cidaris,* we detected a wide range of crystal co- and misorientation. Some stereom sections comprise crystals that have a single crystal-like co-orientation. However, we also detected stereom sections with small-angle misorientations ($< 2°$) and, strikingly, stereom regions that feature a polycrystalline microstructure with large-angle misorientations ranging up to a few tens of degrees. We show with our study how EBSD analysis combined with the pattern matching method can be used to refine the microstructural and crystallographic information obtained for echinoid skeletal elements. To our knowledge, this is the first study applying the pattern matching method to biomineralised hard tissues. It is a technique that might also be useful to understand in greater detail the microstructure of further complex hard tissues, such as bones, teeth and enamel.

Accordingly, based on the misorientation between crystals, we detected that the calcite of the investigated sea urchin species is structured. It can be highly co-oriented; however, it can also be almost untextured with a low crystallographic co-orientation. This is a very surprising finding and demonstrates that sea urchin calcite is not as single-crystalline as previously suggested by many studies [19,32].

2. Materials and methods

2.1. Materials

The study was performed on two species of sea urchins in the class of echinoids, namely *Cidaris cidaris* (Linnaeus, 1758) and *Paracentrotus lividus* (Lamarck, 1816). The sampling area for the specimens is five nautical miles south of Isola d’Elba (Italy) in the central-northern part of the Mediterranean Sea (approx. 42°39′ N 10°17′′ E). The species were collected in May 2014 in the sublittoral zone at 80 – 100 m depth as by-catch from a bottom set net. The sampled seabed consists mainly of coralline algae pebbles (maerl), a typical Mediterranean underwater substrate at dim light conditions [41]. The sea urchins had been air-dried when used for sample preparation.

2.2. Methods

2.2.1. Sample preparation for electron backscatter diffraction

Four *C. cidaris* and four *P. lividus* specimens were dissected to investigate the large primary and shorter secondary spines, as well as the test. The present study examined two primary spines, three secondary spines, and two tests for each species. The spines and the tests were embedded into epoxy resin and were subjected to several mechanical grinding and polishing steps. The final polishing step involved etch-polishing with colloidal alumina (particle size ~ 0.06 μm) in a vibratory polisher. Samples were coated with 4–6 nm of carbon for EBSD analysis, with 5 nm Pt/Pd for SEM imaging. For laser confocal imaging, sample surfaces were not coated.

2.2.2. Secondary electron (SE), backscatter electron (BSE) imaging and electron backscatter diffraction (EBSD) measurements

SE, BSE imaging and EBSD measurements were carried out with a Hitachi SU5000 field emission SEM equipped with an Oxford Instruments NordlysNano EBSD detector and an X-Max 80×80 EDS detector. EBSD scans were taken at 20 kV and were performed with a step size of 300 to 450 nm. EBSD data were evaluated using the Oxford Instruments AZtec and Channel 5 HKL conventional software as well as the Oxford Instruments AZtecCrystal-MapSweeper software. For MapSweeper, the orientation of the EBSD patterns was refined by calcite simulations with the lattice parameters a=4.99 Å, b=4.99 Å and c=17.07 Å. The MapSweeper software implements an efficient pattern matching method for EBSD data evaluation and significantly improves angular precision [30].

Misorientation diagrams report the cumulative misorientation along profiles, i.e. the misorientation compared to the starting point of the profile that functions as a fixed reference. Misorientation values are averaged over five pixels width to enhance data comparability and minimize statistical errors. For the pattern-matched Kernel average misorientation maps, we displayed a range in misorientation between 0° and 2°, with a Kernel filter size of 9×9. For the pattern-matched map in Fig. 2e, the data points display the misorientation to the measurement's average crystallographic orientation. The map, generated with the latter texture component, allows us to see the global influence of structures, such as growth increments, but impedes to visualize local misorientations. Our study is based on 74 EBSD measurements.

2.2.3. Terminology

Subsequently, we define the structural and crystallographic terms used in this article. For additional information on EBSD measurements and data evaluation, see [42].

Microstructure refers to the sizes, morphologies, co- and mis-orientations, and modes of interlinkage of grains. It is shown with colour-coded EBSD maps, where similar colours reflect similar crystal orientations, and different colours highlight differences in crystal orientation.

Pole figures are stereographic projections of crystallographic axes orientations measured for all pixels of an EBSD map or selected areas (subsets). The viewing direction of the pole figure is the same as the viewing direction of the corresponding EBSD maps. All pole figure shown here display the lower hemispheres to ensure they have the same spatial orientation as the corresponding EBSD map. Pole figure show either orientation data points or their density distributions.

Texture or *crystallographic preferred orientation* relates to the distribution of all crystal orientations within a crystallised material. It is illustrated with pole figure. Our study observed two texture modes: (i) a three-dimensionally ordered, single-crystal-like long-range order and (ii) an axial/cylindrical texture.

A *3D single-crystal-like long-range order* is present when clear-cut maxima are observed in the pole figure of all crystallographic axes. Due to the calcitic symmetry, the pole figure of single-crystal-like microstructures show one c-axes cluster and three a*-axes clusters.

An *axial texture* is developed in the relevant material when, in the pole figure, a common crystallographic axis (such as the c-axis) is clustered in a joint orientation and the other crystallographic axes (such as the a*-axes in calcite) are distributed on a circle perpendicular to the texture axis.

Crystal co-orientation statistics are derived from Kikuchi patterns measured at each pixel of an EBSD map. The degree of calcite co-orientation is obtained from measurements of the orientational density distribution, the MUD (multiple of uniform (random) distribution) value. The *MUD* value is calculated by the EBSD software and indicates the crystal co-orientation strength by quantifying in 3D the maximum intensity in the orientational density distribution [43,44]. A high MUD indicates high crystal co-orientation, and a low MUD indicates low to random crystallite orientation. The parameters for data contouring used in this study were fixed to a half width of 5° and a cluster size of 3°. For calcite crystals precipitated from solution at a half width of 5° and a cluster size of 3°, an MUD value of 720 indicates single-crystallinity. In contrast, an MUD value of 1 indicates a lack of preferred orientation and texturing.

The EBSD *band contrast map* depicts the signal strength of the Kikuchi pattern at each measurement point in the EBSD scan. In this study, it is displayed as a grey-scale component and shown with a map. White to light grey colours indicate a high intensity of the Kikuchi signal, corresponding to a high degree of mineralisation. Dark grey and black colours indicate a weak or absent Kikuchi signal, e.g., when scanning organic substances.

Subsets allow us to extract crystallographic data from separated areas of the measured EBSD maps. They can be generated either manually, by selecting specific areas or grains, or automatically, by filtering crystallographic orientations from the pole figure.

When using the EBSD technique for the assessment of structural and chemical information, the collection of the diffraction pattern and the process by which the EBSD pattern is converted into information are critical steps. Two classes of pattern indexing techniques are currently used commercially for a fully automated pattern recognition: (i) the conventional EBSD pattern indexing based on the *Hough transform* [44] and (ii) the new EBSD pattern indexing technique based on pattern matching approaches, which are either implemented using dictionary-like dynamic full pattern matching of test templates [30], or spherical indexing using correlation of spherical harmonic transforms [31]. In the conventional approach, the *Hough transform* [44,45] is used to detect positions of Kikuchi bands. These lines are, then, indexed using crystallographic parameters such as interplanar angles [44]. Depending on the Hough transform settings used for pattern indexing, resolutions in the order of 0.5° to below 0.1° can be achieved, as measured for example by the orientation noise on samples from silicon wafers (see [44,46–48]). When using this method for EBSD pattern indexing in biomineralised materials, however, the angular precision is usually between 0.5° and 1°. The *EBSD pattern matching* approaches rely on a correlation of the complete pattern intensities between the simulated EBSD patterns and the measured EBSD patterns. This mode of EBSD data evaluation renders a significant increase in crystal orientation precision down to 0.01° [29] and can be combined with Hough-based indexing [28,30]. This study uses both types of EBSD data evaluation techniques, in particular, to highlight minute misorientations in sea urchin calcite.

We use the terms *small-angle misorientations* and *large-angle misorientations*. With small-angle misorientations we refer to a misorientation up to 3°-5° that usually occurs within single-crystal-like microstructures of the sea urchin calcite. Large-angle misorientations indicate misorientation above 5° and occurring between adjacent plates or in the polycrystalline parts of tubercles, parapets and spines.

Subsequently, we define biological terms for the sea urchin skeletal elements used in this article; for additional information, see [49–51].

The *stereom* is a crystallised calcium carbonate (in fact, high-Mg calcite) material with a sponge-like structure and appears in modern and fossil echinoderms, such as sea urchin tests and spines. The stereom consists of a mesh of thin cylindrical columns, the *trabeculae*. The stereom has different architectures; it can be *rectilinear* (trabeculae arranged perpendicular to each other), *galleried* (interconnected trabeculae arranged parallel to each other, running in one direction only), or *labyrinthic* (matrix pervaded by ovoid interconnecting pores without internal alignment). *Trabecular extensions* are thin nodes of trabecular columns that run parallel to the morphological long axis of spines and traverse the cortex layer. *Ambulacral* test regions are elongated areas of a test in which the sea urchin tube feet are arranged; *interambulacral* regions are test sections between ambulacra.

Tubercles are ball-and-socket joints forming the attachment sites for spines and pedicellariae to the test plate. They consist of the *basal* boss, the stereom region adjacent to the test, and a *terminal knob*, the outermost tubercular stereom section. *Pedicellariae* are highly evolved and membranous outgrowths connected to the external test surface, where they form the jaws with their pincer-like morphology. Spines are protective mineralised appendages, with the *primary spines* being long and large and the *secondary spines* being small. The *medulla* of a spine is the stereom section that forms the central, co-oriented, portion of the spine. The *cortex* of the spine is the layer that externally encases the medulla from the shaft to the top.

2.2.4. Statistical analysis

The MUD values and misorientation data were calculated automatically by the EBSD software. Misorientation profiles were averaged over five pixels width to enhance data comparability and to minimize statistical errors.

3. Results

This study highlights the microstructure and texture of the *C. cidaris* (Perischoechinoidea) test as well as primary and secondary spines (Figs. 1–10, A1-A5). We complement the structural results gained on *C. cidaris* calcite with microstructure and texture measurements made on *P. lividus* (Euechinoidea) tests and spines (Figs. 11, 12). For both species, EBSD data were evaluated using conventional Hough transformation-based indexing and EBSD pattern matching. To better understand crystal orientation patterns, both species' test and spines were sectioned in two directions (Figs. 1c, A3). Laser confocal microscopy images depict overviews of the surfaces scanned with EBSD and show the site of EBSD scans. The microstructures are visualised with EBSD maps featuring the inverse pole figure (IPF) colouring method with reference direction X (e.g., Fig. 1a). The crystallographic texture is given with pole figure that display the density distribution of the crystallographic c- and a*-axes poles. The crystallographic-structural and biological terminology is defined in the Methods Section (2.2.3) and is illustrated in Appendix Fig. A3.

Fig. 1 gives an overview of EBSD measurements performed on the two cuts through the test of *C. cidaris*. The first cut traverses the entire test from the oral to the aboral side, exposing a circular cross-section of the shell (Fig. 1a, c). The direction of the second cut is perpendicular to the first cut, traversing the interambulacral area of the test from the mouth to the anus of the animal (Fig. 1b, c). The sites of the conducted EBSD scans are displayed on confocal microscopy overview images (Fig. 1a, b). For each EBSD scan, the orientation of calcite crystals is indicated using sketched crystals and pole figure. Many pole figure show multiple density distribution maxima (Fig. 1a), demonstrating that the test comprises different crystallographic units, termed crystal plates. These crystals and/or crystal plates are large, mm-sized, units. In both cuts, adjacent crystal plates vary in orientation and gradually shift in c- and a*-axes orientation (see pole figure in Figs. 1a, b). Calcite c-axes are oriented parallel to the outer test surface and rotate with the outer surface of the test (Figs. 1a, b). Because cut 1 is off-centre from the anal and oral areas, the bottom and top plates appear to be oriented perpendicular, rather than parallel, to the outer test surface (Fig. 1a, b, the corresponding sketched crystals are marked with a red star).

Fig. 2a, b shows a plate; the latter covers the entire thickness of the test cross-section (Fig. 2c). The EBSD scan (Fig. 2a, b) was evaluated with conventional Hough transformation-based data evaluation. We observed the strong mineralisation of the stereom and a high crystal co-orientation strength. We found a uniform orientation in the map and an MUD value of 697 for the entire measurement (Fig. 2b, d). A large area has been scanned (about 1 mm x 600 μm); nonetheless, the strong uniformity in colour (Fig. 2b) indicates only one crystal orientation, i.e. the single crystallinity of the calcite in that stereom portion. Hence, based on conventional EBSD data evaluation, we found a 3D "single-crystal-like" long-range order for that stereom section (see pole figure in Fig. 2d). When the EBSD data set is evaluated with the pattern matching procedure, misorientations within the trabecular growth lines become visible (Fig. 2e). In addition, we observed small-angle misorientations within the stereom; in the map (yellow arrows in Fig. 2e) and in the misorientation diagrams (Fig. 2f). We found misorientations up to about 2° (Fig. 2f). These are, in general, concentrated at trabecular intersections, the junctions where trabeculae meet (indicated with yellow arrows in Fig. 2e). Nonetheless, as the profile C to D in the misorientation diagram of Fig. 2g demonstrates, the calcite within the trabeculae does not seem to be significantly misoriented, even when EBSD data are evaluated with the EBSD pattern matching method (Fig. 2g). This indicates that intratrabecular calcite of *C. cidaris* is well co-oriented.

Fig. 3 and Appendix Fig. A1 visualise the conjunction of crystal plates within the test and their interlaced connection. The colour-coded EBSD maps demonstrate that the interface between the crystal plates has no rectilinear course and that the plates are intricately interlinked. Adjacent stereom crystals are entangled in three dimensions in a complex way, well visible from the intertwining of crystalline trabeculae (Fig. 3a-c). We also found a marked misorientation between adjacent crystals/crystal plates (see misorientation-distance diagrams of Figs. 3c, A1). Although the pole figure show comparable calcite c-axis orientation for neighbouring crystal plates, the misorientation angle-distance diagrams demonstrate a misorientation between adjacent crystal plates of up to 40° (Figs. 3c, A1a). We investigated the degree of misorientation between adjacent crystal plates for the entire circumference of the test. For the circumference through the plates, we found no systematics in misorientation between the crystal plates, e.g., no gradation in misorientation. The misorientation angle between adjacent crystal plates varied arbitrarily between 5° and 40°.

Even though the calcite is highly co-oriented within the plate trabeculae and, thus, in many parts of the test stereom, the calcite of the tubercular terminal knob is polycrystalline. A tubercle is part of a ball-and-socket joint (Figs. 4a, A2a), consisting of a knob-like protuberance where the primary spines are connected to a ring of muscles entwined around the trabeculae of the labyrinthic test stereom (Fig. 4a). The tubercle consists of densely space-filling calcite; within the tubercles, the trabeculae form a dense microperforate stereom network. Towards the interior of the test, the tubercle comprises the terminal knob and the basal boss (Fig. 4a); the latter leads into the stereom of a test plate (Fig. 4a). For the basal boss and the terminal knob, we observed differences in stereom space-filling density and crystal co-orientation strength. Nonetheless, we found a perfectly smooth transition between the different tubercle sections (Figs. 4a, b, A2a, A2b). The stereom of the tubercle has a less regular fabric than the fabric of the stereom of the adjacent test (Figs. 4a, b, A2a, A2b). The crystals at the terminal knob have an irregular morphology and show a high misorientation between each other (Figs. 4a, b, A2a, A2b, EBSD map and corresponding pole figure). For the crystals that form the stereom of the basal boss, we found small-angle misorientations (yellow star in Figs. 4b, A2b). These are

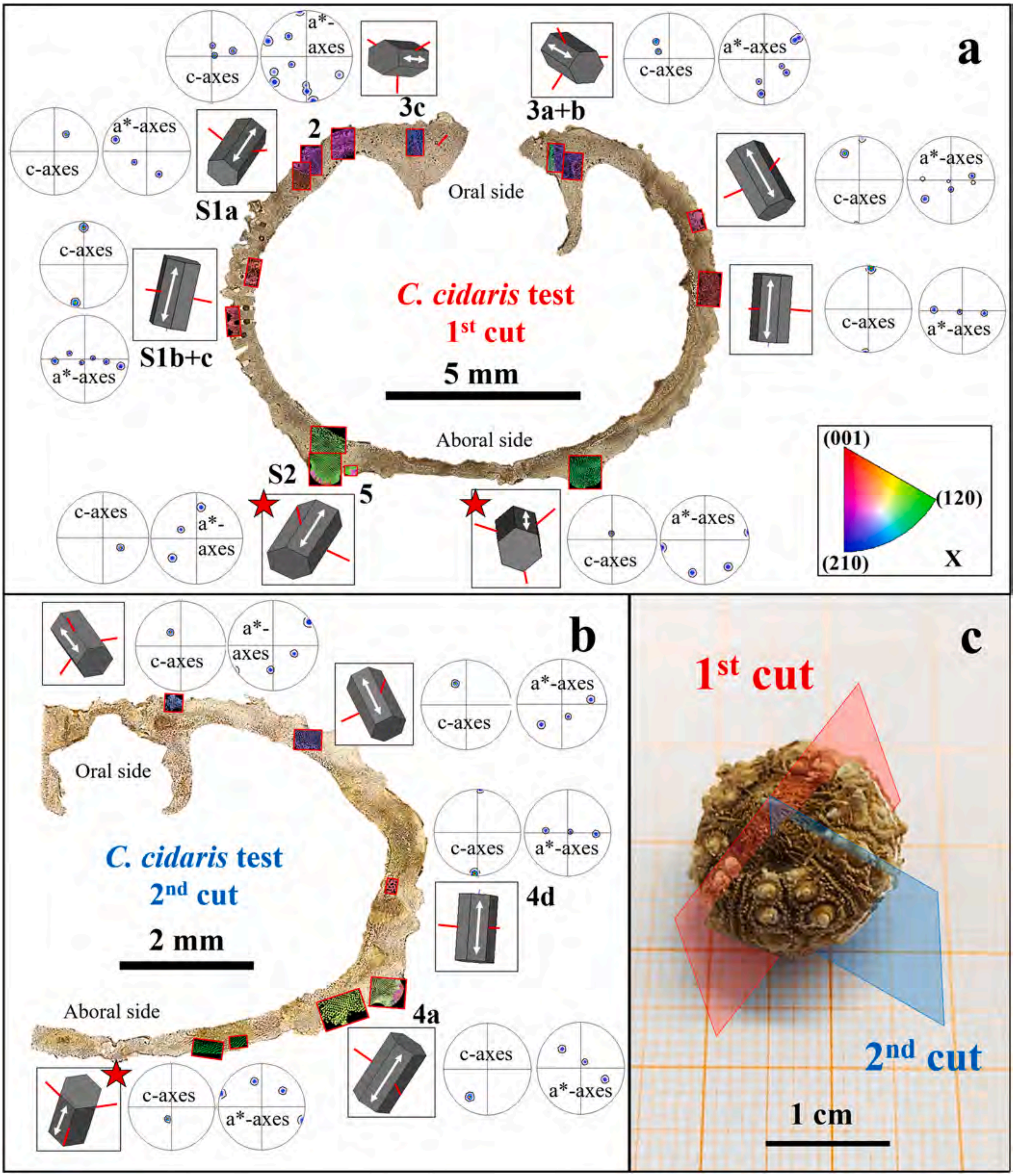

Fig. 1. The texture, calcite c-axis orientation and position of EBSD measurements for two *Cidaris cidaris* tests (a, b), cut in two directions (1st cut, 2nd cut, (c)). Confocal laser microscopy images depict the positions of the performed EBSD scans on the first (a) and on the second cut specimen (b). Density distribution pole figures for c- and a*-axes for selected EBSD measurements show the preferred crystallographic orientation of the plates (a, b). Measurements covering adjacent plates show multiple c-axes orientation maxima in the pole figures; see also Figs. 3 and A1. Sketched crystals visualise the orientation of a*-axes (red lines) and c-axes (white arrows) and demonstrate that the c-axes are oriented parallel to test outer surface. Planes through the *C. cidaris* test indicate the positions of the first (red) and of the second (blue) cut (c). Red stars in (a) and (b) point to those measurements where calcite c-axis orientation does not appear to be parallel to outer test surface. The latter is due to the cut-effect explained in the Results section.

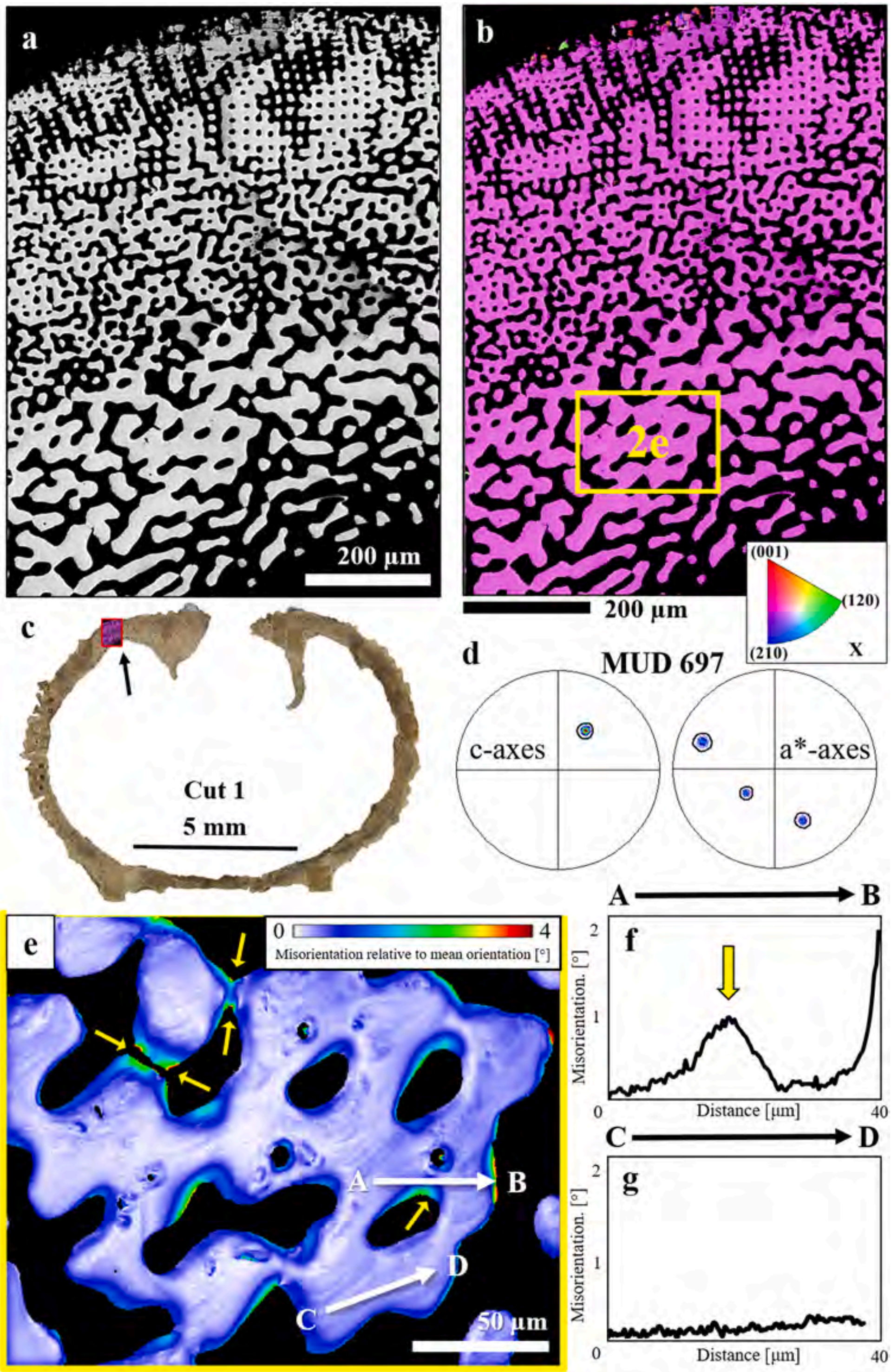

Fig. 2. Microstructure and texture of a *Cidaris cidaris* test plate, covering the entire cross-section of the test (a, b). The measurement was performed close to the oral region of the test sectioned according to the first cut. The EBSD band contrast measurement image (a) and the colour-coded crystal orientation map (b) show two stereom/trabeculae architectures, rectilinear at outer (top of maps) and labyrinthic at inner test layers/sections (bottom of maps). EBSD measurement position is indicated in the laser confocal image (c). The contoured pole figures show a 3D "single-crystal-like" long-range order and a high MUD value of 697 (d). While the measurement shown in (b) was evaluated with conventional EBSD data evaluation, the measurement given in (e) was evaluated with pattern matching. The position of the EBSD scan shown in (e) is indicated with a yellow rectangle in (b). Applying EBSD pattern matching and displaying the texture differences relative to the mean crystallographic orientation of the stereom, we show small-angle misorientations (up to 2°) within the stereom fabric (e). Strikingly, intratrabecular growth increments in the stereom show tiny misorientations that are not observable with conventional EBSD or Kernel average misorientation maps (e). Two misorientation-distance profiles traversing the hard tissue indicate well-observable misorientation maxima along trabecular junctions (yellow arrows in e, f), as well as the high co-orientation of intratrabecular calcite (g).

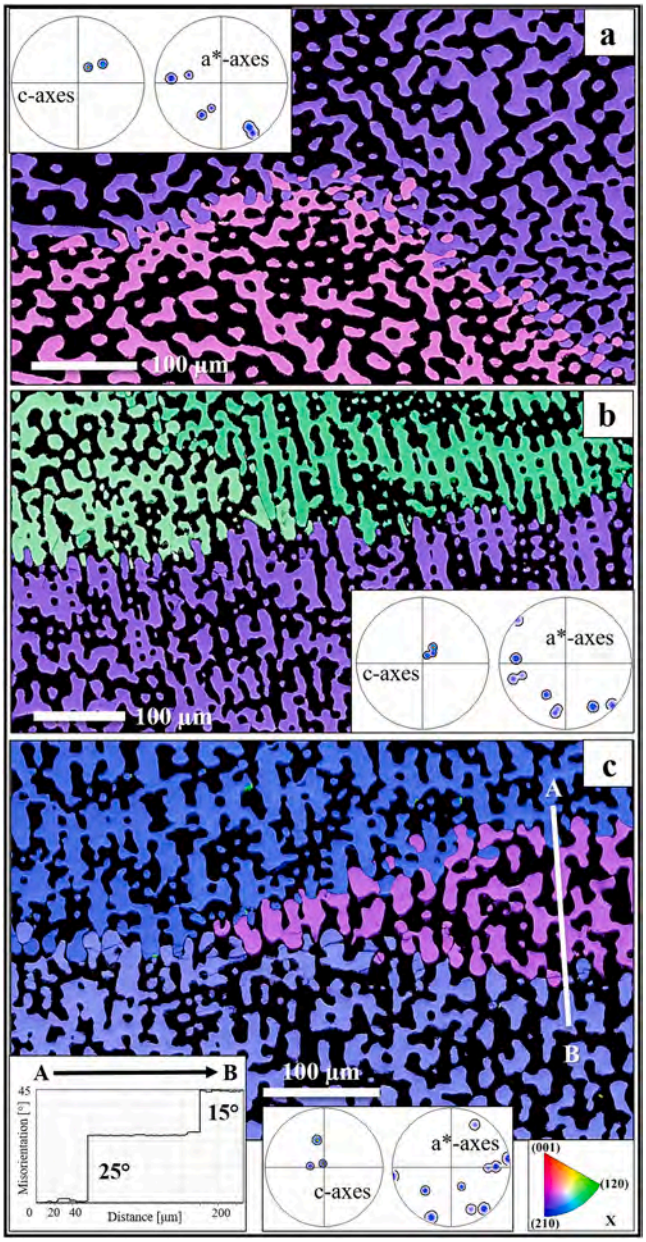

Fig. 3. EBSD scans visualizing the stereom of different test plates of the *Cidaris cidaris* test as well as their interlinkage (a-c). The test was sectioned according to the first cut. The colour-coded EBSD maps are complemented with the corresponding contoured pole figures. The latter display a 3D "single-crystal-like" texture for individual plates. Test plates interconnect along undulated interfaces (a-c). Adjacent test plates are significantly misoriented, at some instances up to 40°; see misorientation versus distance plot in (c). The measurements were evaluated with conventional EBSD data evaluation. The positions of the scans are indicated in the overview of the test in Fig. 1a.

observed only when EBSD data are evaluated with the pattern matching technique and displayed in a Kernel average misorientation map (Figs. 4c, A2c-A2e). These small-angle misorientations are frequent along the trabecular intersections of the microperforate boss and by far surpass the misorientations found in the labyrinthic test plate (Fig. 4d). As the amount of pores in the microperforate tubercle is still very high, the calcite of the tubercle comprises many trabecular junctions and, hence, many small-angle misorientations (Fig. 4c).

While the intratrabecular stereom of the test plates shows a 3D "single-crystal-like" texture with the c-axes oriented parallel to the outer surface of the test, the polycrystalline terminations of the knobs have an axial texture with calcite c-axes oriented roughly perpendicular to the outer surface of the tubercular terminal knob (see the pole figure in Figs. 4a, b, A2a, A2b). We found an MUD of 700 for the test plate (Fig. 4d), an MUD of 665-685 for the tubercular basal boss and an MUD of 79 to 87 for the polycrystalline tubercular terminal knob (Figs. 4, A2).

A similar microstructure to the polycrystalline knob, comprising a polycrystalline as well as a 3D "single-crystal-like" part and termed parapet [52], can be found at the outer shell surface right next to the primary tubercle (Figs. 5a, b). This convex structure encases the tubercle to lock in with the base of the primary spine (Fig. 5b). The polycrystalline parapet has a low degree of crystallographic co-orientation (red star in Fig. 5c-f) and an axial texture that comprises c-axes oriented perpendicular to the outer parapet surface. In contrast, the adjacent 3D "single-crystal-like" stereom is oriented perpendicular to the parapet (orange star in Fig. 5c-e, g). As shown by the pattern-matched misorientation map, apart from a few positions at trabecular junctions, the test is, more or less, free from internal misorientations (Fig. 5e). On the other hand, the polycrystalline parapet shows misorientation streaks (white arrows in Fig. 5e) that run alongside the pores of the microperforate stereom, close to the outer parapet surface.

Most sea urchins form two series of spines: the primary (long) and the secondary (short) spines. For *C. cidaris*, both spines comprise a medulla, the central portion of the spine, and a cortex surrounding the medulla along a large part of the shaft until the tip (Figs. 6, 7, A3). The longer primary and the shorter secondary spines show pronounced differences in the microstructure of their base. The outer base surface of the primary spines has a 3D single-crystal-like long-range order that extends through the co-oriented trabeculae (Fig. 6a). Despite the consistent IPF colouring throughout the basal part of the primary spine, the MUD value scatters at about 670, and the pole figure reveal angular deviations (Fig. 6a). This indicates that primary spine stereom calcite is highly co-oriented, nonetheless, as it comprises low angle misorientations, it cannot be addressed as single-crystalline. However, up to now, there is no agreement from which value of mosaic-spread a single crystal should no longer be termed a single crystal but a polycrystalline entity. For secondary spines, the basal part is not strictly co-oriented and features large (~100 µm diameter) outer surface regions of polycrystalline material (Fig. 6b-d). Data refinement by EBSD pattern matching revealed many internal small-angle boundaries in the crystals along the microperforate outer spine layer. These form misorientations between 0.5-1.5° (Fig. 6d). Towards the highly co-oriented, labyrinthic stereom of the medulla, intratrabecular misorientations are significantly decreased (Fig. 6d).

In *C. cidaris*, the cortical layer of the primary spine has a rough surface. We found aggregations of crystals forming spiky longitudinal crests along the outermost cortex surface (Fig. 7a, b). The cortex surface of secondary spine tips is rather smooth and significantly less structured than the surface of primary spines (Fig. 7a, b). At the outer edge of the primary/secondary spine shaft, the connection between the medulla and the cortex becomes visible (Fig. 7a, b). Their interface is uneven; multiple thin series of pores continue from the medulla into the cortex (Fig. 7b). The crystallographic c-axes in the 3D "single-crystal-like" medulla (yellow star in Fig. 7b) are parallel to the direction of the shaft. The polycrystalline cortex (white star in Fig. 7b) has an axial texture with calcite c-axes being aligned more or less perpendicular to the c-axes of the medulla (Fig. 7b). Towards the tip of the spine; the outer spine surface becomes increasingly serrated (Fig. 7a, b).

We obtained similar structural-crystallographic characteristics for *C. cidaris* secondary spines (Fig. 7c, d). The highly co-oriented medulla (red star in Fig. 7d) interlocks in a complex way with the weakly axially textured polycrystalline cortex (white star in Fig. 7d). It appears that *C. cidaris* secondary spines have a smoother outer surface when compared to the outer tip surface of the primary spines (Figs. 7, A4). The stereom of both the primary and the secondary spine medullae is galleried (for definition, see Terminology section 2.2.3) with large, interconnected pores (Fig. 7a-d) that appear to continue into the

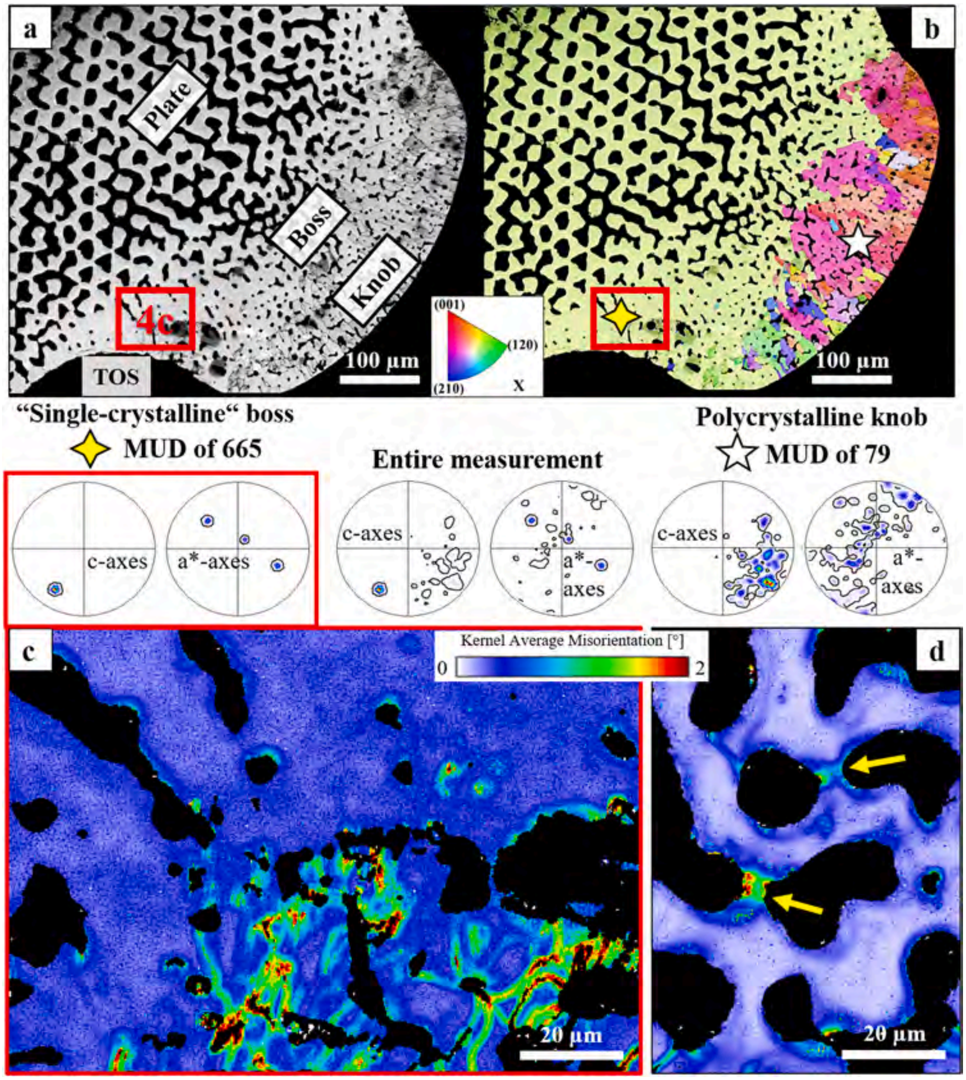

Fig. 4. Crystal assembly architecture and the bimodal texture of tubercular calcite at the aboral region of the test of a *Cidaris cidaris* specimen. As visible from the band contrast measurement (a) and the colour-coded orientation maps (b), the tubercle comprises a co-oriented section (yellow star in b) and a strongly misoriented, polycrystalline region, the latter being along the tubercle outer surface (TOS, white star in b). The contoured pole figures show the texture for the boss and knob of the tubercle as well as for the entire measurement (a, b). The orthogonality in calcite c-axis orientation between the stereom of the boss and the plate and the tubercle knob is well visible. The measurement shown in (a, b) was evaluated with conventional EBSD data evaluation. Pattern matching EBSD data evaluation applied to a subset of the tubercle (c) reveals the presence of many small-angle misorientations (1° to 2°) within the boss, and near the terminal knob (c). At trabecular intersections of a measurement located in the core of the plate (yellow arrows in (d)), misorientations can reach 2° to 3°. Misorientations for the trabeculae near the terminal knob are higher than in the core of the plate (d). The positions of the EBSD scans can be retraced from Fig. 1b; the area of the close-up map (c) is marked with a red rectangle in (a, b).

adjacent cortex (e.g., Fig. 7b). Nonetheless, the outermost 50 µm of both types of spines is rather formed of microperforate (for definition see Terminology section 2.2.3) calcite.

Fig. 8 highlights two spines sectioned in different cuts close to their base. A primary spine was sectioned perpendicular (Fig. 8a, b) and parallel to its morphological long axis (Fig. 8c), and a secondary spine was cut parallel to its morphological long axis (Fig. 8d-e). The distinctness in microstructure and texture between the medulla and the cortex is well visible. The stereom of the medulla comprises trabeculae arranged in radial lines (Fig. 8a, b) and with calcite c-axes oriented parallel to the direction of the shaft (sketched crystal and pole figure in Fig. 8a). Directly adjacent to the cortex, the crystal network of the medulla is continuous and imperforate (yellow arrows in Fig. 8a). Sectioned perpendicular to the long axis of the spine, the crystals of the cortex are elongated (Fig. 8c). Rather than forming a sheath with a constant extent that surrounds the stereom of the medulla, the crystals of the cortex are grouped into longitudinal crests (red arrows in Fig. 8b, c). However, these do not cover the entire outer stereom surface evenly. High-spatial resolution EBSD scans visualise the complex internal structure of a primary spine longitudinal crest (Fig. 8c). In secondary spines, the texture and microstructure of the shaft appear similar (Fig. 8d-f). The cortex has an axial texture with crystallographic c-axes preferentially oriented perpendicular to the outer spine surface (Fig. 8e). In contrast, the medulla is formed of a galleried, highly co-oriented calcite stereom that is mostly imperforate along the interface with the cortical layer. Thus, for all investigated spine specimens of *C. cidaris*, the crystallographic texture of the cortex is perpendicular to that of the medulla (Fig. 8b, c, e).

4. Discussion

4.1. Test and spine stereom architecture

In cidaroid tests and spines, various stereom architectures are

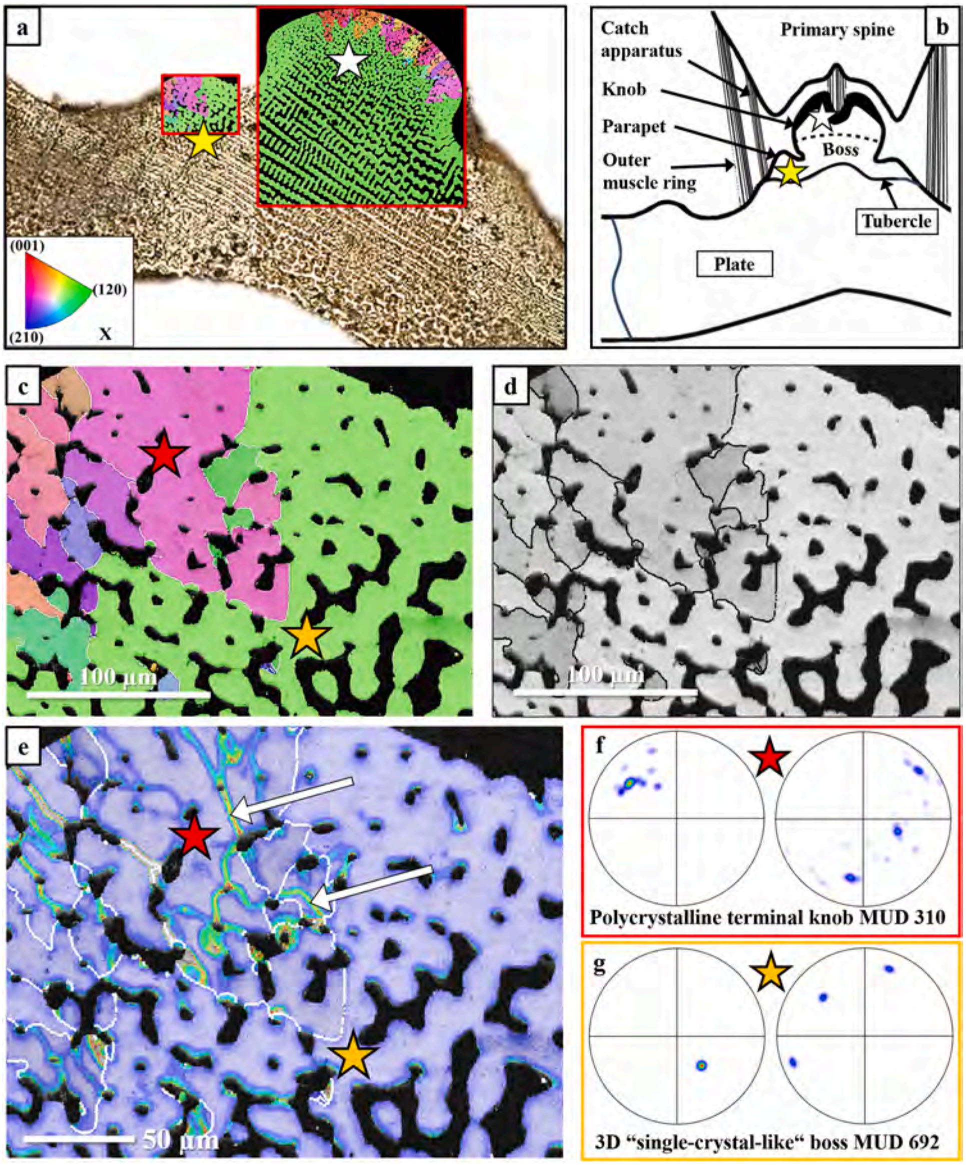

Fig. 5. Microstructure and internal misorientations of a parapet located next to a primary tubercle, where the muscle ring attaches to the *Cidaris cidaris* test (a, b). Terminology and spine attachment are depicted in a schematic illustration (b). EBSD data were evaluated with conventional EBSD data evaluation (c, d) and pattern matching (e). Analogous to Fig. 4c, d, the pattern-matched measurement is displayed as a Kernel average misorientation map between 0°-2° (e). Pole figures show colour-coded data points of the two subsets (f, g). Similar to the terminal knob of primary tubercles (Figs. 4c-e, A2), the microstructure of the parapet stereom (red star in c) differs from the labyrinthic stereom of the inner test plate (orange star in c). The trabeculae follow a tighter meshwork that leaves smaller pores and is formed of an assembly of polycrystals (a, b). Aside from the grain boundaries, the stereom comprises many internal misorientations that are particularly frequent at trabecular junctions and can well be detected by EBSD pattern matching (c). The polycrystalline parapet has an axial texture with the c-axes clustered in an orientation perpendicular to the outer parapet surface (d), while the calcite of the test plate is co-oriented and can be considered to be 3D "single-crystal-like" (e). Misorientation streaks are frequent in the polycrystalline parapet (white arrows in e).

developed, depending on the species and the region in the skeletal element [53,54]. We found rectilinear, gallieried, microperforate and labyrinthic stereom architectures (for the definition of the fabrics, see Terminology Section 2.2.3). For *C. cidaris*, the distribution of different stereom fabrics in the test is less homogenous than described by Smith [50]. Instead, the distribution of the above-named stereom fabrics is localised to certain regions of the test and/or the spines.

The internal section of the ambulacral and interambulacral test plates with the attached tubercles comprises an irregular pattern of large pore channels, and trabeculae called the labyrinthic stereom fabric [50, 55]. This stereom fabric is abundant in sea urchin plates; Wainwright et al. [4] described the labyrinthic stereom as the main architectural design element of sea urchin tests and spines. At central regions of the ambulacral and interambulacral plates, the stereom is streaked with extensive trabeculae; elongated pore channels tend to form one-directional galleries with perpendicular struts. Reaching the tubercle, the ordered stereom fabric of the test decreases in porosity and pore size. The large pore channels are replaced by very small and irregularly arranged pores, and a microperforate dense fabric forms the stereom of the tubercles. A rectilinear stereom architecture, creating the basal boss of the tubercle, as suggested by Smith [50], could neither be seen with FE-SEM, nor confocal laser microscopy imaging. However, a rectilinear stereom was observed along the outer section and surface of the test plate. Galleried stereom occurs in the test near the tubercles, however, it is far less abundant in the test of the investigated *C. cidaris* species than reported by Smith [50].

The spines of *C. cidaris* have varying stereom fabrics at their base, shaft, and tip. The spine shaft can be subdivided into the medulla and

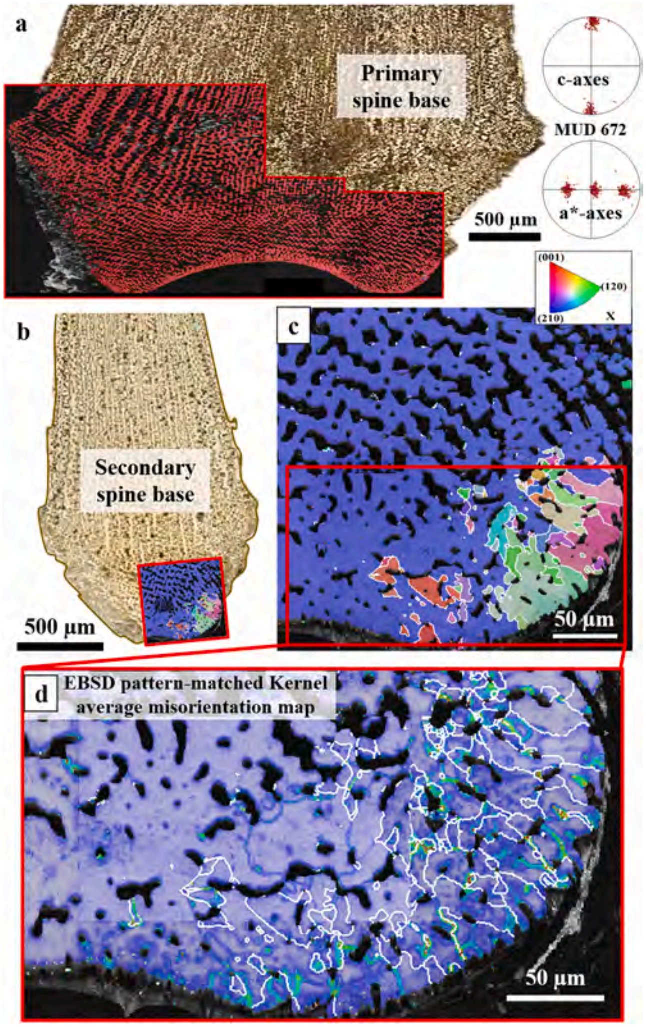

Fig. 6. Microstructure and texture of the basal portion of *Cidaris cidaris* primary and secondary spines visualised with laser confocal images (a, b) and EBSD maps (a, c, d), with conventionally evaluated EBSD data (a, c), and with EBSD data evaluated with pattern matching (d). Analogous to Fig. 4c, d, the pattern-matched measurement is displayed as a Kernel average misorientation map between 0°-2° (d). For primary spines, the calcite of the entire basal stereom is co-oriented (a). The stereom architecture changes from microperforate along the outer spine surface to galleried in the medulla (a). At the basal outer surface of secondary spines, where the muscle ring attaches to the basal section of the spine, we found a spine portion formed of irregularly-shaped and misoriented crystals (c). EBSD pattern matching revealed many small-angle misorientations within the crystals as well as in the microperforate stereom along basal spine outer surface.

cortex, each with a distinct pore architecture. In the shaft, the stereom in the medulla is microperforated along the outer spine surface and rather galleried and lamellar on the inside. The linearity and co-orientation of the pore channels seem to increase towards the cortex. In the basal region of the spine, the microstructure of the medulla is primarily labyrinthic, and the pore channels continue into the outer base surface. An identical internal architecture was observed for the cidaroid *Prionocidaris baculosa* (Fig. 1 in Dery et al [56]). For this species, the stereom fabric is predominantly labyrinthic at the base of the spines. However, along the outer base surface of the spines of *P. baculosa*, the stereom fabric seems to be less perforate than in the core region of the spine.

Smith [50,57] suggested that the change in stereom architecture in the test and the spines might be closely related to functional aspects. The above-described anisotropic arrangement of trabeculae and pore canals increases the test plate's resistance to bending stress [58]. Grossmann

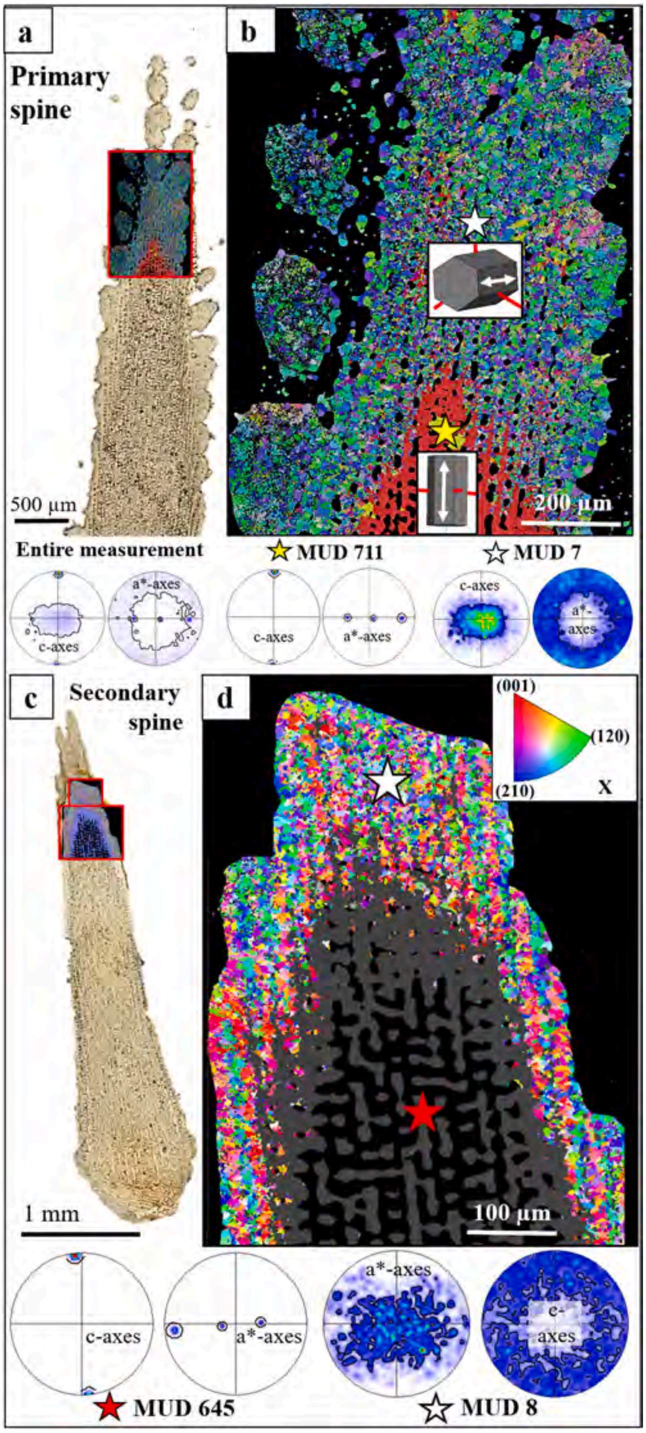

Fig. 7. Microstructure and texture at the tip of *Cidaris cidaris* primary and secondary spines (a-d). EBSD measurement positions are indicated with the confocal laser microscopy images (a, c), EBSD data were evaluated with conventional EBSD data evaluation. For the primary spine (b), the colour-coded EBSD map and the corresponding pole figures indicate a single-crystal-like microstructure and texture for the medulla for the spine (yellow star in (b)), while for the cortex (white star in (b)) we observed a polycrystalline microstructure and texture. As shown with the sketched crystals in (b) and well visible from the given pole figures, crystal orientations of the cortex are perpendicular to that of the stereom. Secondary spine tips have comparable microstructure and texture, as observed for primary spine tips (b, d). We found for both, primary and secondary spines, an immense difference in MUD value and, hence, crystal co-orientation strength for the medulla (MUD: 711, 645) and the cortex (MUD: 7, 8) of the spine.

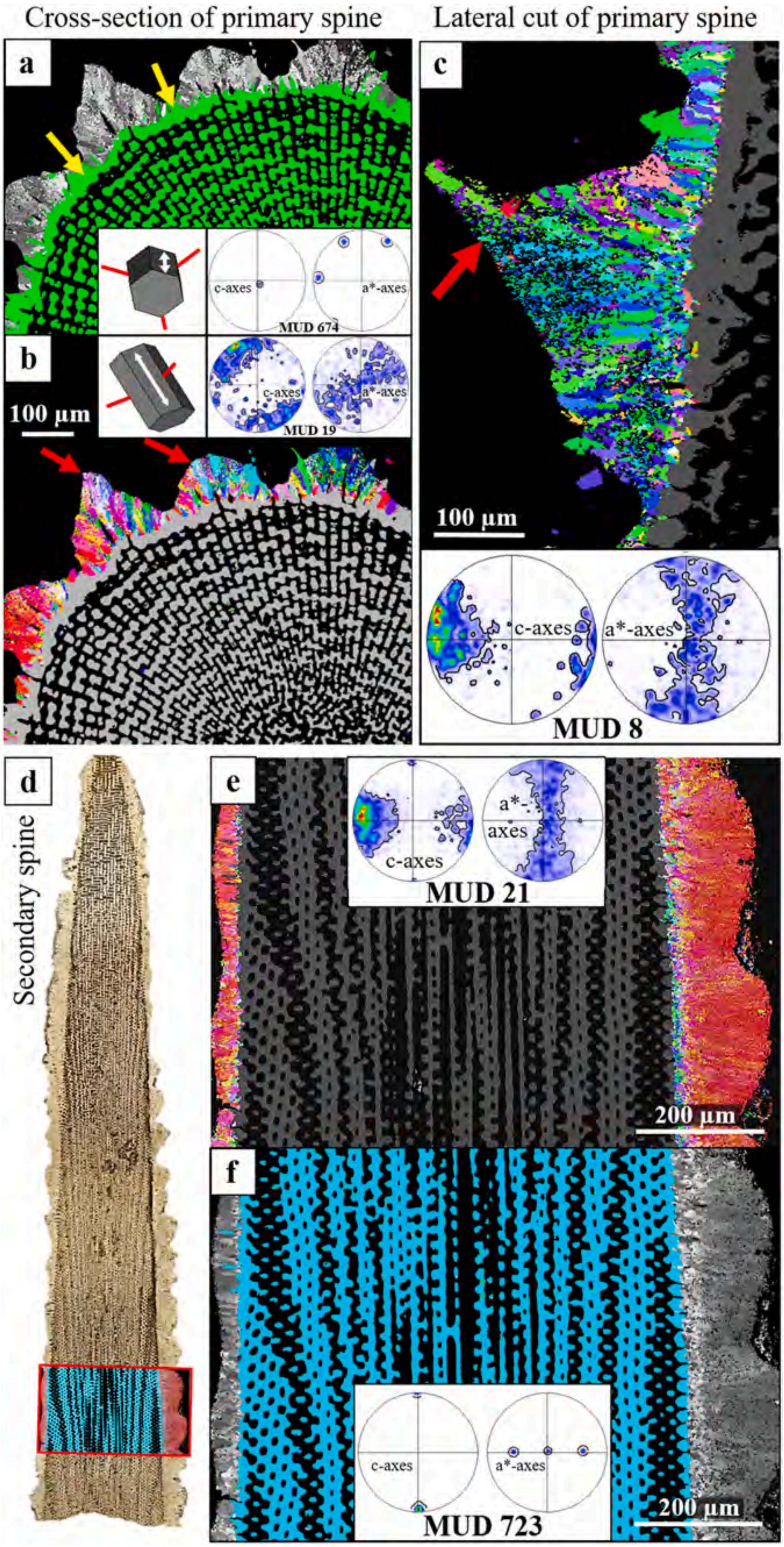

(caption on next page)

Fig. 8. Microstructure and texture of *Cidaris cidaris* spine medulla and cortex along the shaft of the spine (a-f), for a primary (a-c) and secondary (d-f) spine and cross (a, b) and lateral (c-f) sections through the spine. EBSD data were evaluated with conventional EBSD data evaluation. The stereom of the medulla is galleried. A three-dimensionally imperforate tube of calcite is present at the interface of the stereom of the medulla with the adjacent cortex (yellow arrows in a). Along the cross-sectional (b) and the lateral cut (c) through primary spines, the cortex forms longitudinal crests (red arrows in b, c). Despite their polycrystalline microstructure, the calcite of the longitudinal crests has an axial texture with the c-axes being oriented perpendicular to the c-axis of the medulla (sketched crystals in a, b). In secondary spines (d), the microstructure of the cortex gradually shifts from low to high crystal co-orientation. In contrast, the central part of the secondary spine has a single-crystal-like long-range order (f).

and Nebelsick experimentally confirmed structural implications for the stereom differentiation [59]. According to Grossmann and Nebelsick [60], the chaotic distribution of struts in the stereom also impedes crack propagation. Stress-transfer capacity was reported by Tsafnat et al. [61] using micro-computed tomography. Through simulations, high-stress concentrations occurred at specific points in the test and spine's architecture, where brittle cracking would most likely happen [61]. Connective tissue within the porous microstructure of the stereom, enhanced by orientation and gradation of the pores in interplay with organic and possibly amorphous interfaces, would lessen stress concentration and enable a more even stress distribution [58,62,63].

4.2. Crystallographic arrangement of calcite in the test and the spines

4.2.1. The primary and secondary spines

The calcite of *C. cidaris* spines is formed with two crystal textures. The medulla of the base and the shaft have a 3D single-crystal-like long-range order. In contrast, the cortex at the outer tip of the spine is a polycrystalline aggregate with a low preferred crystallographic orientation. The c-axes of the medullar trabeculae are oriented parallel to the morphological long axis of the spine [20,64], while the c-axes of the cortex crystallites are oriented perpendicular to that of the longitudinal medullar trabeculae. The texture difference between the spine cortex and the medulla results from different mineralisation processes. The texture of the medulla is mainly controlled by biological factors predetermining its microstructure and texture. In contrast, the growth process of the cortex is largely influenced by competitive growth determinants evoking the formation of the axial texture of the cortex crystals. The lack of crystallographic continuity and the compactness of the micro-perforated cortex stereom are interpreted as important factors in enhancing the structural stability of the spine [56]. The cortex comprises sub-μm sized crystallites with a varying degree of crystal co-alignment.

The changeover from the highly co-oriented medulla to the polycrystalline cortex is intricate. As visible from the subset analysis for the tip of two secondary spines (Fig. 9), the single-crystal-like framework of the medulla continues into the cortex (Fig. 9a). Exposing thin lines of tiny trabeculae (white star in Fig. 9a) that run parallel to the morphological long axis of the spine, subsets of the EBSD measurement in Fig. 9a show the extension of the medulla up to the outer surface of the spine tip. It should be noted that the cross-sections of the extended medullar trabeculae are significantly smaller in the spine tip than the cross-sections observed in the monophasic medulla. The medullar/trabecular extension maintains the crystal orientation of the highly co-oriented medulla, and the medullar/trabecular lines run parallel to the morphological long axis of the spine, irrespective of their position in the spine (Fig. 9a).

The extensions of the medulla play a significant role in the crystallisation of the cortex. The polycrystalline cortex is subdivided into two subsets with similar crystal orientation patterns (Fig. 9b, c). Each subset has its crystallographic c-axes oriented perpendicular to the medulla as well as to one another (see sketched crystals in Fig. 9a, b, c). Rather than being randomly distributed within the cortex, the subset maps of the cortex show that the two sets of crystal orientation (set 1 and set 2) align in strict lines (Fig. 9b, c) and that these run parallel to the lines of the medullar extension (Fig. 9a). Therefore, the microperforate tip of the cortex has a 3D microstructure with a clear-cut and ordered crystal orientation pattern and the arrangement of the crystallites that form the very tip of the cortex is not random. The tip of the cortex comprises thin parallel entities where the medullar extensions (Fig. 9a), the first orientational set of crystals (set 1, Fig. 9b) and the second orientational set of crystals (set 2, Fig. 9c) alternate in a lamellar fashion. Based on the linear and ordered arrangement of the medullar/trabecular extensions and on the two ordered sets of crystals inherent to the cortex, it can be assumed that the extended medullar stereom functions as a nucleation substrate for the small cortex crystals. The trabeculae of the medulla that extend into the cortex and function as nucleation surfaces have a morphology resembling spheres. Thus, the cortex crystals that nucleate on these surfaces grow in all directions perpendicular to the trabecular morphological long axis (see the large scatter of data in the pole figures in Fig. 9a, b). This explains the lack of crystallographic co-orientation within the two sets of crystals, despite their axial texture (Fig. 9b, c).

A similar pattern can be observed for a further secondary spine tip that also shows a clear-cut relationship between the medullar/trabecular extensions and the crystallographic orientation pattern of set 1 and set 2 of the cortex (Fig. 9d, e). Similar to previous measurements, the medulla has a 3D single-crystal-like long-range order (Fig. 9d). The medullar/trabecular extensions forming a framework of thin, parallel lines (Fig. 9d) function as the nucleation surface for cortex crystal growth (Fig. 9e). Thus, the cortex appears to feature multiple crystal entities with similar orientations that stretch parallel to the morphological long axis of the spine, up to its outer tip surface (Fig. 9e). The c-axes orientation of cortex crystals scatters broadly perpendicular to the medullar orientation. It can be concluded that the microstructure and crystallographic texture of the cortex crystals are determined by the surface configuration of the extended trabeculae of the medulla; their growth process is largely influenced by competitive growth determinants [65].

Considering that a competitive growth process determines the microstructure of the cortex layer crystals, it is fascinating to find that this process can lead to the complex serrated and undulating outer spine surfaces observed for *C. cidaris* (e.g., Figs. 7, 8). Our results indicate that the outer surface of the medulla is rarely perfectly smooth and conical. As overview measurements suggest, the medulla rather forms longitudinal crests with angular outlines (Fig. A4). Indeed, the thin trabecular extensions of the medulla can predetermine the thickness, morphology and outer surface of the entire cortex layer. Even when considering that their small thickness partly appears from the cut that sections them more and more tangentially, the trabecular extensions still vary from the microstructure of the inner medullar stereom. Observable at regular distances along the cross-section of a primary spine (Fig. A5a), the medullar extensions form fan-like extensions (white arrows in Fig. A5b, c). Similar to the tip of the spine, this framework of fan-like extrusions is filled with fine-grained crystals, oriented perpendicular to the extension of the medulla (see pole figure in Fig. A5b, c). This specific microstructural arrangement in the upper shaft and tip of the spine and within the longitudinal crests may be a unique way for the organism to optimise two aspects of the outer spine surface:

(i) Generating a porous framework that functions as a nucleation template for the cortex and allows the organism to crystallise sophisticated spine morphologies, such as the longitudinal crests, at low metabolic cost.

(ii) Compared to the relatively weak stereom that can promote crack development [21], the thin encasing cortex can better dissipate cracks in its polycrystalline microstructure, thus optimising the

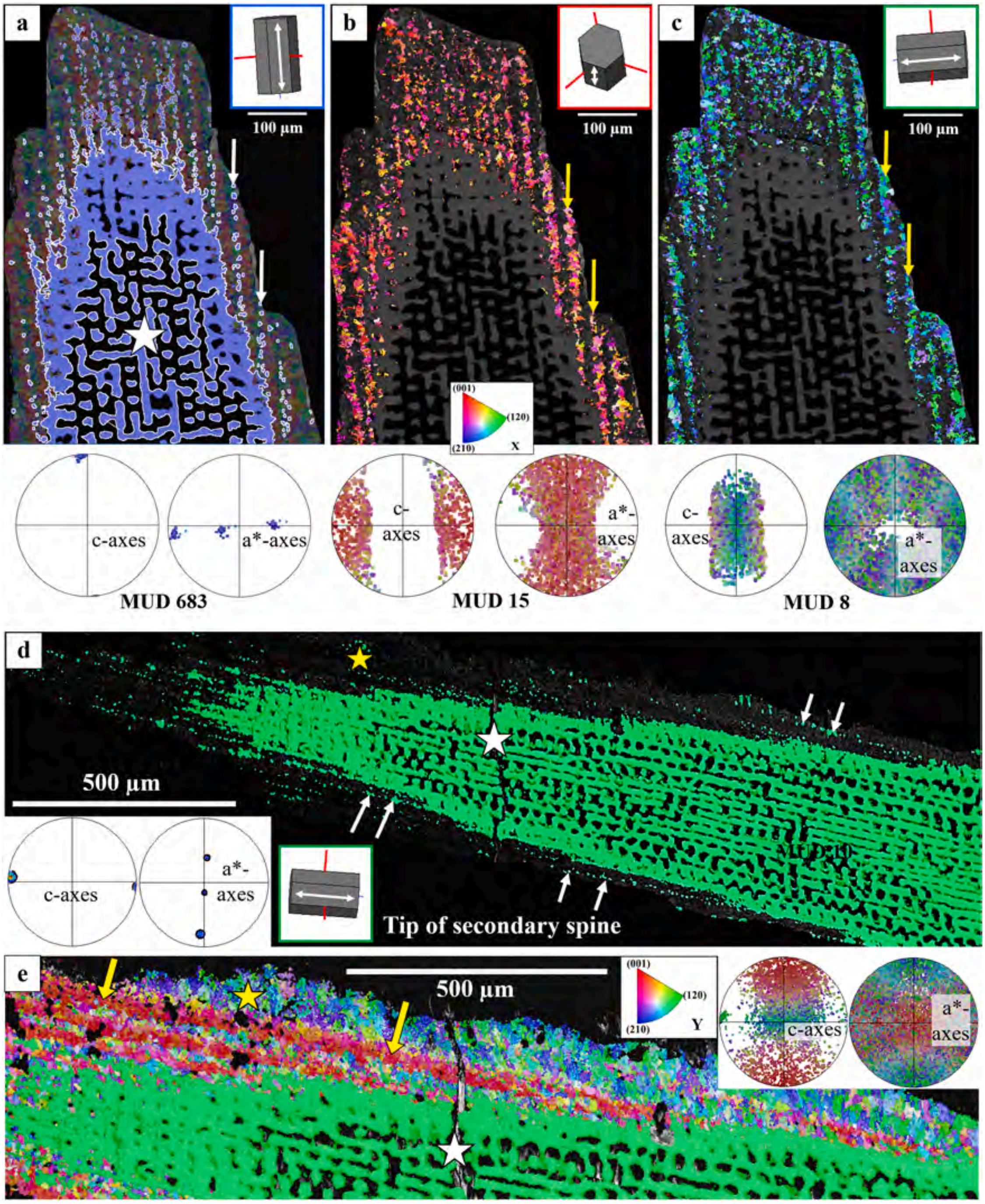

Fig. 9. Microstructure and crystallographic texture of *Cidaris cidaris* spine medulla and medullar extensions (white stars arrows in a, d) and of the first-formed cortex crystals at the very tip of the spine (yellow arrows in b, c, e). EBSD data were evaluated with conventional EBSD data evaluation. The competitive growth microstructure of the cortex shaft is already well observable close to the tip of the spine (yellow stars in d, e). At its very tip, the spine cortex consists of medullar extensions (white arrows in a, d) and two sets of first-formed crystals (yellow arrows in b, c, e). Set 1 and set 2 cortex crystals are differentiated from each other by their orientations, both of which are orthogonal to the orientation of the medullar trabeculae as well as to each other. This is indicated by sketched crystals (a, b, c) and/or the colours of the set 1 and set 2 crystals (red and blue; coding for orientation (yellow arrows in b, c, e)). The medulla consists of a galleried stereom, formed of co-oriented calcite (white star in a, d, e). Small trabeculae (medullar extensions) are organised in parallel series (white arrows in a) with similar crystallographic orientation as the calcite of the medulla (white arrows and pole figure in d). The extending trabeculae (white arrows in a, d) are significantly thinner than the trabeculae of the galleried stereom of the medulla (white star in a, d, e). Polycrystalline sheets of granular crystals (b, c) enclose the medullar extensions, and form the cortical crystals. The latter crystals have an axial texture and a low co-orientation strength. The c-axis orientation of the set 1 and set 2 crystals is always perpendicular to the axes of the medullar extensions; the two sets of crystals are ordered in parallel lines (yellow arrows in b, c, e).

spine's toughness without losing the energy absorption properties of the stereom [9]. For the latter, two microstructural characteristics are important: (1) the small size of most cortex crystals leads to many grain boundaries. These can block dislocation and crack development in biological as well as man-made materials [66]. (2) The c-axes orientations of the cortex crystals are generally oriented orthogonal to the outer spine surface. Previous studies investigating the azimuthal variability of mechanical properties in biomineralised tissues showed that the hardness increased when measurements were performed on materials with crystal c-axes perpendicular to the tested surface [67,68]. Accordingly, even though the microstructure of the cortex crystals appears to be driven to a large extent by a competitive growth mechanism, the previously described specific texture is also relatable to material function, i.e. to some degree it is biologically determined.

The competitive growth mechanism that influences the texture and microstructure of the cortex is also obvious from the spine shaft, where the nucleation surface provided by the trabeculae of the medulla is smooth (Figs. 8d-f, 10). The texture of the first-formed cortex crystals at the spine shaft is broadly axial; however, their co-orientation strength is low, as indicated by MUD values between 50 and 70. Towards the outer spine shaft cortex surfaces, crystal sizes (from ~20 μm^2 to around 200 μm^2; see Fig. A5a-c) and crystal co-orientation strength (see MUD values in Fig. 10) increase, and crystal orientation becomes more and more coherent with distance away from the medulla. These structural characteristics point to a microstructure determined by growth competition. At crystal formation through growth competition, many crystals nucleate close to each other and, at growth, compete for space. Due to the anisotropic growth kinetics of calcite, the likelihood for a small crystal to grow into a large entity and to outcompete its neighbours depends on its crystallographic orientation. It is inversely related to the deviation of the crystal's growth direction (c-axis) from an orientation normal to the nucleation template. The growth competition process results in a substantial decrease in the number of crystals, an increase in crystal size and the generation of a progressively stronger crystallographic preferred orientation as one moves away from the nucleation substrate (Fig. 10b, c). Calcite c-axes in the outer cortex shaft of *C. cidaris* are almost parallel to each other, and the texture reaches MUD values up to 220 (Fig. 10). Nonetheless, the crystals at the outer cortex are still significantly more misoriented than the crystals that form the highly co-oriented medulla, where we found MUD values of about 660 to 700. We conclude that since the medulla or its trabecular extensions function as nucleation surfaces for the growth of the cortex, the smoothness of the outer medullar surface defines the arrangement and crystallographic texture of the cortex crystals.

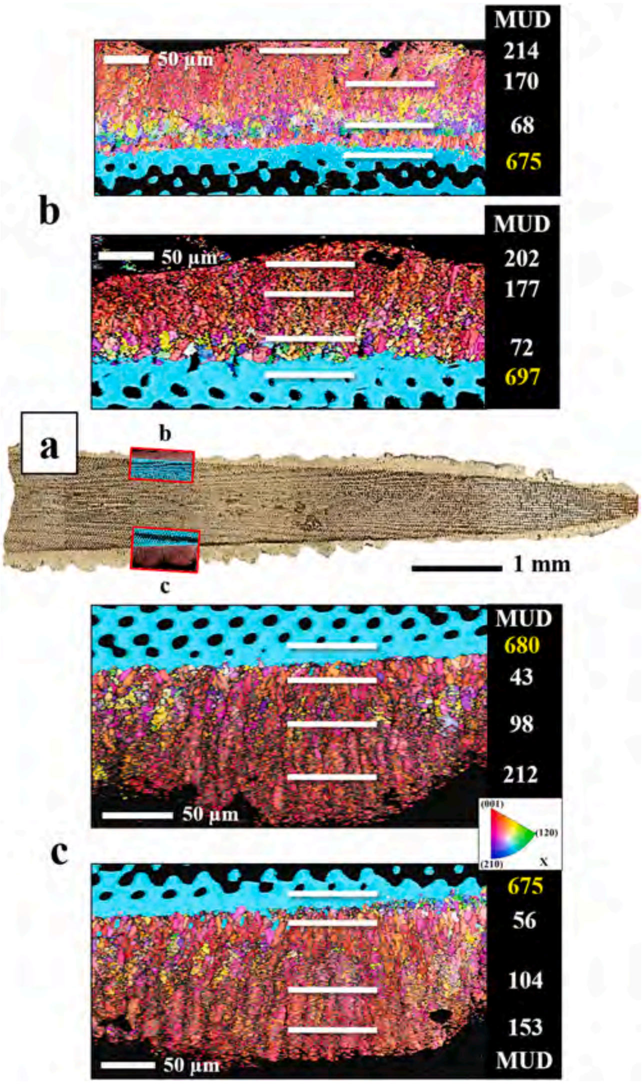

Fig. 10. Calcite crystal co-orientation strength, expressed with MUD values, for the medulla and for the cortex along the shaft of a *Cidaris cidaris* secondary spine (a-c). The position of EBSD scans is given with a confocal micrograph (a); measurements were performed on opposing sides of the outer spine surface. The calcite of the stereom of the medulla is co-oriented, showing MUD values between 675 and 700 (b, c). The calcite of the first-formed cortex crystals is significantly less co-oriented (43 < MUD < 72), however, their co-orientation strength increases towards the outer spine surface (153 < MUD < 214) (b, c). EBSD data were evaluated with conventional EBSD data evaluation.

Since trabecular extensions run parallel to the morphological long axis of the spine, they are most apparent at the tip of the spine where their close spacing is best visible (Fig. 9). The cortex crystals nucleating from the trabecular/medullar extension framework, therefore, spatially restrict themselves in three dimensions (Figs. 7, 9, A5d-A5f). This impedes the growth of large crystals and generates the particular microstructure and irregular crystal morphologies that we observed for the cortex at spine tips. In contrast, the cortical layers along the shaft of the spines show lack of trabecular/medullar extensions. This generates a rather smooth outer nucleation surface for the growth of cortex crystals, although the topography of the inner stereom, per se, is very intricate. Due to the lack of trabecular extensions blocking the crystallisation pathway away from the medulla, the cortex crystals at the shaft can grow competitively, increasing in size and crystallographic co-orientation. For secondary spines, we found that the cortex occupies only for the upper third of the entire spine's outer surface (Fig. A6a). The onset of the cortex is directed by a ring-shaped medullar bump that follows the orientation of the trabeculae (yellow star in Fig. A6b). It is imperforate and has a thickness of up to 50 μm, comparable with the thickness of the adjacent cortex (Fig. A6b). Below this bump, the outer surface of the secondary spines is defined by a co-oriented microstructure that resembles the microstructure of the medulla (Fig. A6c). However, rather than forming a galleried stereom, the pore size decreases towards the outer spine surface; this outermost hard tissue is usually imperforate (Fig. A6c). We conclude that even though the microstructures of the spine cortex differ significantly for the tip and shaft of the spine, the crystal growth process is consistent throughout the entire cortex. With the cortex of the spine, we observed, for the first time for a carbonate biological hard tissue, two different configurations of the competitive growth process: (1) an initial and (2) an advanced growth configuration, predetermined by the surface structure of the nucleation template and facilitated by the available space for the growth of crystals.

4.2.2. *The test*

The *c*-axis orientation of the calcite plates in the test is tangential to the outer test surface, as reported by Raup [18], who identified the crystallographic orientation in coronal plates of *C. cidaris* using optical light microscopy. The results of the EBSD measurements in this study agree with the relation between the crystallographic orientation of this echinoderm calcite and its test morphology, as shown by Raup [18]. The c-axes of the calcite crystals within the test plates follow the curvature of the outer test surface in the aboral side's direction (Fig. 1). Several hypotheses have been proposed to explain why some sea urchin tests show this characteristic; however, its functional significance is still unknown.

Raup [14,18,69] assumed that the preferred crystallographic orientation of the c-axes might be related to environmental adaptions. According to this theory, light-sensitive echinoids could utilise the anisotropic transmission properties of calcite to adapt to shallow, sunlit environments and block unwanted sunlight. However, no correlation could be found between the crystallographic organisation of the test and the habitat [15]. It is more likely that the preferred c-axes orientation is important for plate curvature and, thus, controlled by the secreting epithelium [15,70] or results from developmental constraints during growth [17].

The test plates feature single-crystal-like stereom frameworks slightly tilted to each other along the test profile. The axial co-orientation strength within the test plate varies between MUD values of 661 and 716. As a reference, synthetically grown calcite single crystals have an MUD value of 712 [43] and 725 [71]. Strikingly, the highest abundance of individual test plates was detected on the oral side near the masticatory apparatus. Each section is structurally locked by interconnecting trabecular extensions as described by Seilacher [72], Hidaka and Takahashi [73] and Smith et al [74]. Misorientation angles between neighbouring sections vary between 15° and 45°.

Exceptional for both cuts through the shell and both investigated sea urchin species is the polycrystalline rim of the primary tubercles (along the terminal knob) at the aboral side (Figs. 4, 11). The tubercle rim resembles a polycrystalline aggregate with an axial texture. The longitudinal axes of the tubercle crystals are oriented perpendicular to the single-crystal-like plate and the outer tubercle surface. The crystallites are limited to the denser microperforate stereom fabric (Figs. 4a, b, A2a, A2b). The 3D “single crystal-like” plate contrasts with the

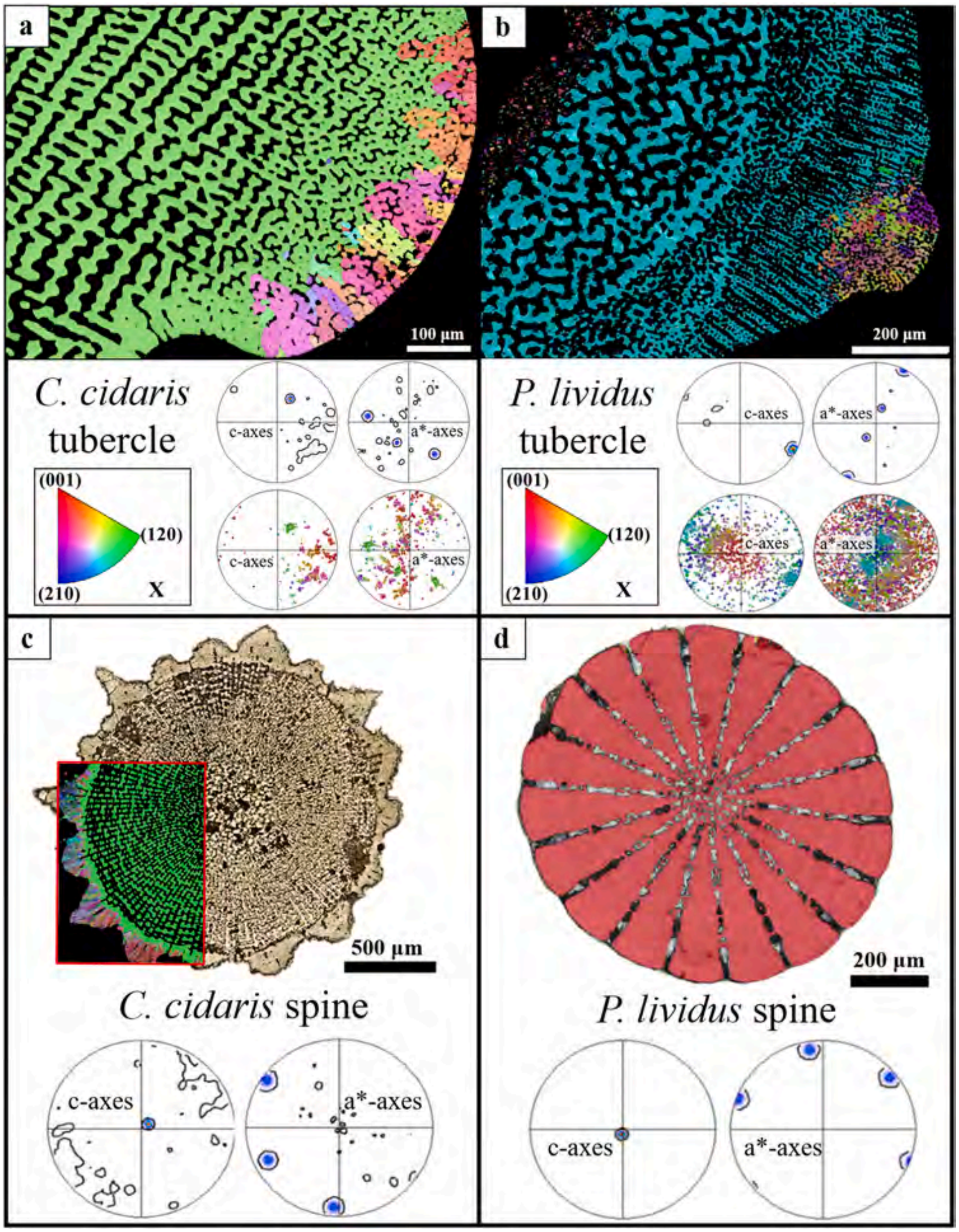

Fig. 11. Comparison of microstructure and texture characteristics between *Cidaris cidaris* and *Paracentrotus lividus* tubercle (a, b) and spines (c, d). EBSD data were evaluated with conventional EBSD data evaluation. The colour-coded EBSD maps of *C. cidaris* (a) and *P. lividus* (b) visualize the interlinkage between the highly co-oriented calcite of the plate and that of the polycrystalline knob of primary tubercles. The polycrystalline terminal knobs keep the porous stereom structure of the plate, however, differ strongly in their crystallographic texture (a, b). EBSD scans were performed on the cross-sections of *C. cidaris* (c) and *P. lividus* (d) primary spines. *C. cidaris* spines feature a polycrystalline cortex surrounding the single-crystalline medulla (c). *P. lividus* spines do not have a cortex; instead, they are formed of co-oriented stereom calcite at the spine base that merges into radially arranged, dense wedges (d).

polycrystalline boss, which lacks crystal orientation continuity. While this bimodal-like texture pattern could also be found in the base of secondary spines (Fig. 7b-d), it was not observed for the base of the primary spines (Fig. 7a). Okazaki et al [23] reported a similar polycrystalline microstructure using crystal etching and decoration. Their study showed no correspondence between the c-axes of the tubercle and the c-axes of the spine base, indicating that the two structures develop independently from each other. Donnay and Pawson [20] mention that the rotating spine on the tubercle tip, connected by a ball-and-socket joint, has a grinding action. The mechanical stress breaks off small bits of skeletal material, which will fuse to a polycrystalline structure during growth [23,75]. Our results indicate that for both the tubercle, the parapet and the secondary spines (Fig. 5), the polycrystalline regions do not disrupt the porous architecture of the stereom but rather continue it up to the outer shell surface (Figs. 5, 6, A2). Similar to the cortical layer in primary and secondary spines, the axial texture of the polycrystalline knob runs perpendicular to the single-crystal-like plate. This shows that the tubercle crystals are not randomly oriented. Their orientation follows a directed growth process that might result from growth competition.

In summary, our study shows the interesting properties of calcite microstructure and texture at the sea urchin terminal knob of tubercles, parapets and along the outer sections of the spine base. These sections consist of calcitic trabeculae, their growth and organisation is strongly biologically determined. Nonetheless, calcite microstructure and texture are distinct from the rest of the test or spine. We found large crystals (mean area: 800 μm^2) with dendritic morphologies and calcite c-axes oriented perpendicular to the skeletal element and orthogonal to the calcite orientation of the adjacent test or spine. These skeletal portions, the terminal knob of the tubercle, the parapet and the surface of the base of the spine, are located near muscle attachment sites (Figs. 5, A3). Valved marine organisms develop a specific crystal microstructure and crystal texture at the sites where the muscles attach to the valves. As shown for other shelled organisms, e.g. for bivalves [76,77] and brachiopods [78], it appears that at muscle attachment sites of echinoids as well the crystals adjacent to the tendon cell layer of the attaching muscles often feature large entities. These crystals generally have their c-axes oriented perpendicular to the surface of the skeletal element (this study and [62–64] and, most probably, for a strong attachment, parallel to the collagen-rich fibrils that leave the focal adhesions of the muscle cells. Although the shell-muscle attachment varies between echinoderms and bivalves or brachiopods, it is interesting to observe that across different phyla, the presence and attachment of muscles seems to influence and manipulate the microstructure of biological hard tissues.

4.3. *Comparison of calcite microstructure and texture for sea urchin species living in the same habitat*

C. cidaris is a specimen representing the Cidaroidea, a subclass of the Echinoidea. First EBSD measurements on the *C. cidaris* test and skeletal elements were reported by Förster [51]. A different subclass of Echinoidea is the Euechinoidea; this subclass includes most sea urchin species living today. First EBSD measurements are reported by Alsheikha [79] for the test and the spines of the euechinoidean sea urchin *Paracentrotus livididus. P. lividus* is a well-studied organism [21,80–82] and lives in shallow waters in the Mediterranean Sea. *C. cidaris* and *P. lividus* often coexist, however, occupy different subareas of the same habitat.

In contrast to the crystallographic pattern of the test of *C. cidaris* (Fig. 11a), *P. lividus* exhibits c-axes orientation perpendicular to the test plate's outer surface (Fig. 11b). Test plates in *P. lividus* mainly comprise a single-crystalline-like labyrinthic stereom fabric. The microstructure of the boss varies significantly, with galleries running perpendicular to the test surface (Fig. 11b). The terminal knob of the tubercle comprises a polycrystalline aggregate that is not limited to the tubercle rim, as it is the case for the tubercle of *C. cidaris*. This might indicate differences in the muscle-tubercle attachment configuration for the two investigated sea urchin species.

The studies of Alsheikha [79] and Varkoulis et al [82] reveal a compact microstructure of the spine shaft and tip of *P. lividus* that strongly contrasts the perforate stereom of *C. cidaris* spines (Fig. 11c, d). The spines of *P. lividus* comprise tightly spaced wedges, the septa, which increase in thickness towards the outer spine surface feature a 3D single-crystal-like long-range order (Fig. 11d). The porous zone between the wedges is narrow in cross-section and appears uniformly thick. Longitudinal cuts through the two species' primary spines highlight differences in microstructure of the spine basal area. The primary spines of *C. cidaris* comprise a labyrinthic medulla with many small-angle misorientations, particularly along the trabecular junctions (Fig. 12a, d). In contrast, the basal part of *P. lividus* spines comprises a galleried, single-crystal-like stereom on the inside of the spine and a microperforate stereom along the spine's outer surface (Fig. 12b, e). The spine base, shaft and tip show crystallographic texture continuity, and the microstructural changeover between the basal stereom and the imperforate septa is smooth in *P. lividus* spines. The crystallographic orientation of the *c*-axes follows the orientation of the long axis of the spine (Fig. 12c, f). In contrast to *C. cidaris*, the spines of *P. lividus* lack a polycrystalline, weakly co-oriented cortex.

Hence, although living in the same habitat, *C. cidaris* and *P. lividus* exhibit differences in texture and microstructure of both the test and the spines. The presence of a cortex and the highly porous microstructure in *C. cidaris* spines, compared to those of *P. lividus*, are striking features and might yield advantages in resilience to, e.g., stress distribution, hard tissue regeneration and other structural attributes.

4.4. *The single crystalline character of the sea urchin test and spine*

The 3D "single crystal-like" stereom of the plates and the medulla of the spines of *C. cidaris* show a strong axial co-orientation strength with MUD values ranging from 662 to 723. As mentioned in section 2.2, laboratory-grown calcite single crystals have MUD values between 712 [43] and 725 [71].

Authors who used conventional EBSD measurement and data evaluation report that sea urchin spines are single crystals [21]. However, as demonstrated in this study, small misorientations are not detected with conventional EBSD measurement and data evaluation. An exception to the latter is formed by the study of Goetz et al [80,83]. Based on high-resolution EBSD measurements and, in particular, a specific EBSD data evaluation, the authors could show minor orientation differences of up to 0.1° within the septa of the sea urchin *Amblypneustes pachistus* [83]. While the polycrystalline nature of sea urchin skeletal elements has previously been suggested by other authors, such as Seto et al., Cölfen et al., and Goetz et al. [24,26,80], the combination of high-precision EBSD and the pattern matching method used in the presented study shows for the first time the presence and distribution of small-angle misorientations. Rather than using an image transform, the latter method tests for each point in the measured EBSD map dynamical pattern simulation with precise calibration parameters [30]. Through EBSD pattern matching, we detected that the orientation precision of EBSD measurements for biological carbonate hard tissues becomes significantly improved to an angular precision of less than 0.1° compared to the 0.5° to 1° angular precision with the standard Hough-transformation-based EBSD data evaluation method [44].

4.4.1. *The small-angle misorientations in the C. cidaris test*

High-resolution misorientation maps and profiles show that *C. cidaris* shells comprise considerable misorientations in both test plates and spines (e.g., Figs. 2e-g, 4c, d, 5d, 6d, 12d and A2c-e). We observed large-angle misorientations (more than 5°) in the polycrystalline parts and small-angle misorientations (up to 3-5°) in the single-crystal-like sea urchin calcite (see Terminology section 2.2.3). In the plates, the inner trabeculae usually have a high crystallographic co-orientation (MUD values >700). This is indicated by whitish colours in the high-resolution

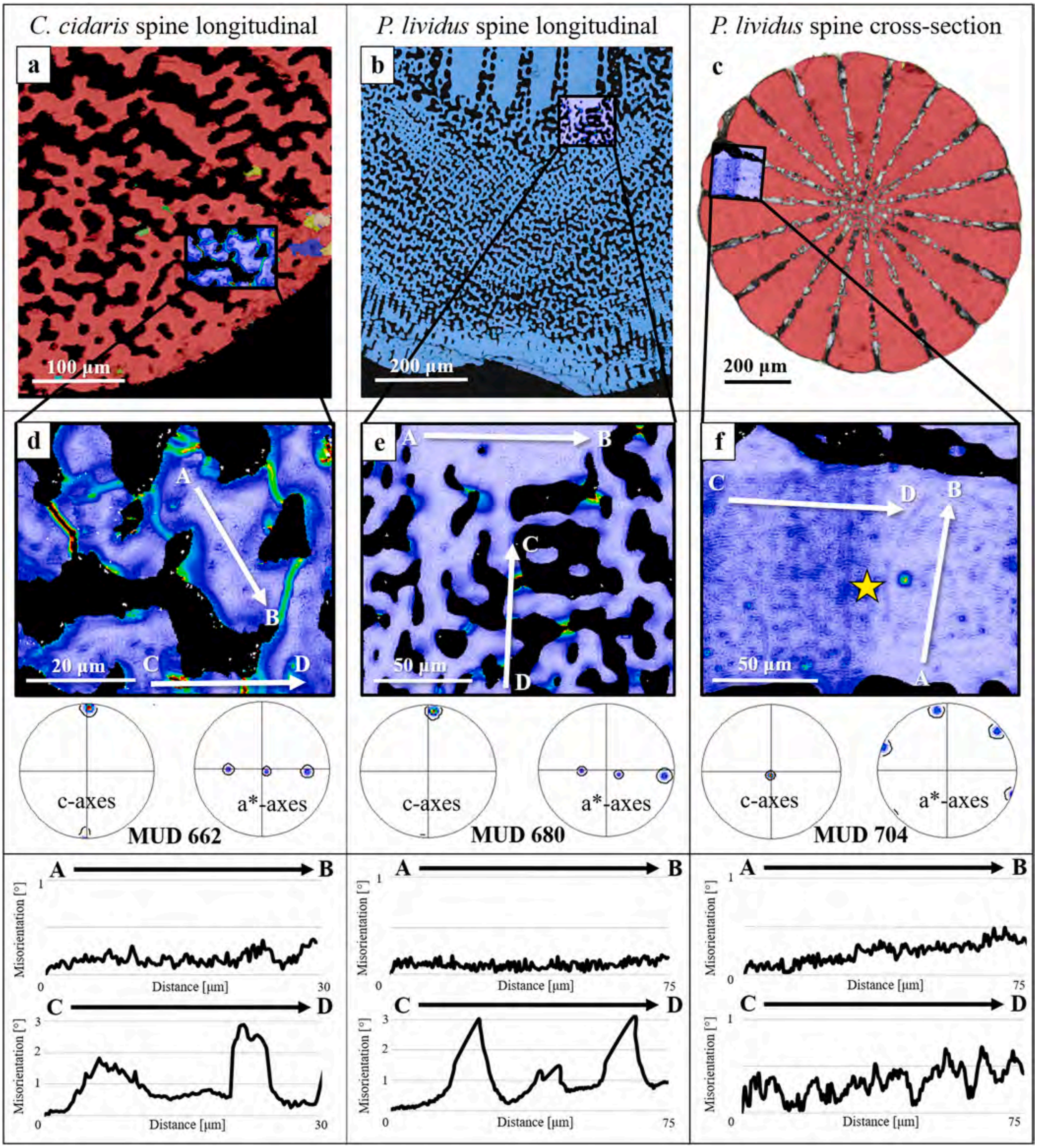

Fig. 12. Comparison of internal misorientations between *Cidaris cidaris* and *Paracentrotus lividus* spines. EBSD data were evaluated with conventional EBSD data evaluation (a-c) and evaluation using pattern matching (d-f). Colour-coded EBSD overview maps (a-c) show the spine microstructure and the position of the maps that were evaluated with pattern matching (d-f). Analogous to Fig. 4c, d, the pattern-matched measurements are displayed as Kernel average misorientation maps between 0°-2° (d-f). The pattern-matched EBSD maps are complemented with contoured pole figures and misorientation versus distance profiles (d-f). In the stereom of *C. cidaris* and the basal spine part of *P. lividus,* misorientations in the trabeculae are low (<1°). High misorientations, up to 3°, are present at the connecting bridges between the trabeculae (d, e). The dense wedges of *P. lividus* are highly co-oriented and only show small misorientations up to 0.5° (f). The yellow star in (f) highlights a region with increased misorientation frequency that runs laterally to the spine septa of the *P. lividus* spine cross-section.

EBSD maps (e.g., see arrow visualizing the trajectory location of profile C to D in Fig. 2e) and with the cumulative misorientation profiles (e.g., Figs. 2e, g, 4d). We consider the inner trabeculae to be more or less single-crystalline.

Due to the perforate character of the stereom framework, the test plates have a large interior surface. Angular misorientations predominantly appear along the trabecular junctions, reaching misorientation angles up to 2° (Fig. 2e, f, 4d). Our study shows that the regions with low-angle misorientations between crystals are not evenly distributed along the skeletal element surface; they are particularly frequent for pore cross-sections with strong curvatures (yellow arrows in Fig. 4d). Since the labyrinthic stereom comprises many trabeculae that simultaneously grow in different directions, it is common that trabeculae converge and interconnect. However, strongly curved interconnection surfaces may interfere with the stereom organisation, which is responsible for the advanced mechanical properties observed for the sea urchin hard tissue [58]. Thus, the misoriented areas might result from the organism's attempt to counteract structural instabilities that result from the generation of the labyrinthic stereom framework. This behaviour has been recently suggested for the echinoderm stereom in the starfish *Protoreaster nodosus*, regarding the misorientations as a by-product of the complex skeletal formation process that strives for the optimisation of the hard tissue mechanical performance [8,84].

Our high-resolution EBSD measurements indicate that the crystallographic co-orientation of the different stereom fabrics is not similar. For example, differences in the misorientation angle distribution become visible when comparing the microperforate stereom near the tubercular boss (Fig. 4c, A2c-A2e) with the labyrinthic stereom located in the centre of the same test plate (Fig. 4d). The latter shows, in general, small misorientation angles for intratrabecular regions or the trabecular connections (Fig. 4d). However, in the microperforate section near the outer shell surface, the Kernel average misorientation is significantly higher. This is particularly well observable in the central part of the trabeculae, where the microperforate stereom has an average local misorientation of ~0.5° versus ~0.1° in the labyrinthic stereom (Fig. 4c, d). The microperforate stereom near the tubercle features streak-like regions of internal misorientations (1-2°) that appear to connect the pores and traverse the stereom (Fig. 4c). These frequently occurring misorientation streaks could result from deformations caused by high stresses acting on the tubercle due to muscular activity. However, the exact origin of this feature, which also occurs in the muscle attachment region of primary spines (see Fig. 12a, d) is not yet understood and needs to be analysed in more detail.

4.4.2. Comparison of the single-crystallinity of *C. cidaris* and *P. lividus* spines

Angular misorientations near sharp pore surfaces of a 3D "single-crystal-like" stereom are not limited to the plates of the test; they are also frequent in the spines of *C. cidaris*. Near the base, the primary spines of *C. cidaris* form a labyrinthic stereom of co-orientated trabeculae; here, we find significant misorientations along the trabecular junction surfaces (Fig. 12a, d). The misorientation profiles in the pattern-matched EBSD measurements (Fig. 12d) indicate that the intratrabecular spine sections are well co-oriented with a cumulative misorientation angle below 0.5°. Even though, the spines cannot be considered to be single-crystalline due to the high misorientation angles of up to 3° towards the trabecular surfaces and intersections (profile C to D in Fig. 12d). The lack of orientational continuity is, furthermore, apparent from the rather low MUD value of 662 of the spine (Fig. 12d).

In contrast to *C. cidaris*, the stereom in *P. lividus* primary spines does not extend from the base to the tip but gradually shifts into septa starting upwards from the shaft. In the basal areas of *P. lividus* spines, the stereom appears to be galleried, with the channels somewhat aligned longitudinally to the growth axis of the spine (Fig. 12b). While in *P. lividus* crystallographic misorientations within trabeculae and the dense septa are very low (<0.3°), the stereom also features scattered areas with high misorientations (up to 3°, Fig. 12e). Nonetheless, these are far less widespread in *P. lividus* spines, compared to *C. cidaris* spines. Two misorientation profiles traversing the septa both longitudinally and perpendicularly show that the misorientation distribution differs within the cross-section of the spine (Fig. 12c, f). Perpendicularly (profile A to B in Fig. 12f), misorientations appear regular and have a cumulative misorientation angle below 0.5°. Longitudinally, from the outer spine surface towards the medulla (Profile C to D in Fig. 12f), cumulative misorientations fluctuate periodically; the point-to-point misorientations are significantly higher than the ones for the lateral profile. Differentiated regions of enhanced misorientation lateral to the growth direction of the septa (yellow star in Fig. 12f) and the periodic misorientations crossing the septa indicate different growth spurts from the inner to the outer spine surface. Thus, the hard tissue crystallised in the same growth spur is highly co-oriented; however, the hard tissue that crystallised at different growth spurs comprises considerable misorientations. Our results not only demonstrate the polycrystallinity of sea urchin calcite, but also show that the degree of internal misorientation varies depending on the stereom fabric and thickness of the respective trabeculae. A similar effect has recently been observed with SAXS and WAXS studies on different stereom fabrics in *Cidaris rugosa*: The authors report a polycrystalline structure with a varying degree of internal co-orientation that might be caused by differences in trabecular order [85].

Applying misorientation profiles or texture component maps to pattern-matched EBSD maps allows us to see long-range changes in crystallographic orientation compared to a reference point. Both the *C. cidaris* and the *P. lividus* stereom show gradual rotations of the crystallographic axes. This becomes obvious from cumulative misorientation profiles (white arrows in Fig. 12d, e, f) and is also observable in greater detail in texture component maps (Figs. A7, A8). For a *C. cidaris* tubercle (Fig. A7) and a *P. lividus* spine (Fig. A8), the texture component maps yield cumulative misorientations up to 2°. For the microperforate boss in *C. cidaris*, some trabeculae even have an orientational divergence of 4° compared to the mean orientation value of the measurement (Fig. A7). It should be noted that, surprisingly, these gradual misorientations seem to accumulate towards a specific direction in the structural element. For the tubercle, the number of misorientations increases towards the outer knob surface (Fig. A7), and for the spine, it increases parallel to the morphological long axis of the spine (Fig. A8).

In essence, the EBSD pattern matching method allows us to detect minute misorientations within biomineralised tissues with great orientational precision. The measurements performed for the test plate, tubercle, and the primary spines of *C. cidaris* and *P. lividus* show a consistent pattern between stereom organisation and small-angle misorientations.

(i) The highest degree of crystallographic co-orientation was observed for the dense, imperforate septa of *P. lividus* (Fig. 12e, f). These structures can be considered single-crystalline. Local misorientations of more than 0.1° are uncommon, as there is a lack of major pores in the network, i.e., there is an absence of trabecular junctions within the biomineralised tissue.

(ii) For the perforate stereom fabrics such as the galleried or the labyrinthic stereom (Figs. 2e, 4d), the crystallographic co-orientation depends on the distribution and interconnection of the trabeculae. The inner trabecular hard tissue is highly co-oriented; however, trabecular intersections creating sharp curves might cause significant misorientations. The latter may arise from the organism attempting to interconnect the differently aligned trabeculae and to smoothen pore surfaces for structural stability.

(iii) The highest degree of misorientation was observed in the dense and microperforate stereom fabrics near the outer surfaces of the test and of the primary spines (Figs. 4, 12d). Due to decreased ordering and size of the pores, as discussed in section 4.1 of this study, the biomineralised tissue is traversed by many misorientation streaks that reduce the strength of co-orientation (indicated by the MUD value) of the calcite. These streaks are not yet well-understood. They may either stem from internal or/and external stresses exerted on the outer shell surfaces of the test and of the spines. They also might be due to the increased amount of small-sized pores, relative to the inner plate of the test.

(iv) Our study shows that the test plates and spines in *C. cidaris* are not perfectly single-crystalline. Not only do they have polycrystalline calcite assemblies at the tubercles, parapets, spine base and cortex of the spines, but the 3D "single-crystal-like" biomineralised tissue of these skeletal elements comprises, in addition, cumulative misorientations features of up to 3° or even more.

5. Conclusions

The echinoid species *C. cidaris* forms a high-Mg calcite skeleton, with the mineralised parts consisting of a test, primary and secondary spines and the chewing apparatus. The test comprises an assembly of crystal plates and their tubercles (Figs. 1, 4). The test microstructure is a 3D meshwork of thin bands or columns, the trabeculae, which interconnect at junctions. The microstructure of the spines comprises a central medulla, formed of a network of trabeculae, and a cortex, composed of a polycrystalline assembly of small crystals that encase most of the spine shaft up to the tip (Figs. 13, A4).

This contribution highlights and discusses the crystallography, microstructure, and texture of the *C. cidaris* test and spines. Results are based on high-resolution EBSD measurements and sophisticated EBSD data evaluation using the pattern matching method. For the first time, for biological hard tissues, we show how this method can be used to obtain precise microstructural and textural information for biomineralised materials such as echinoid skeletal elements. Of central interest for the presented study is the assessment of misorientations within the crystals that form the stereom of the test, the tubercles and

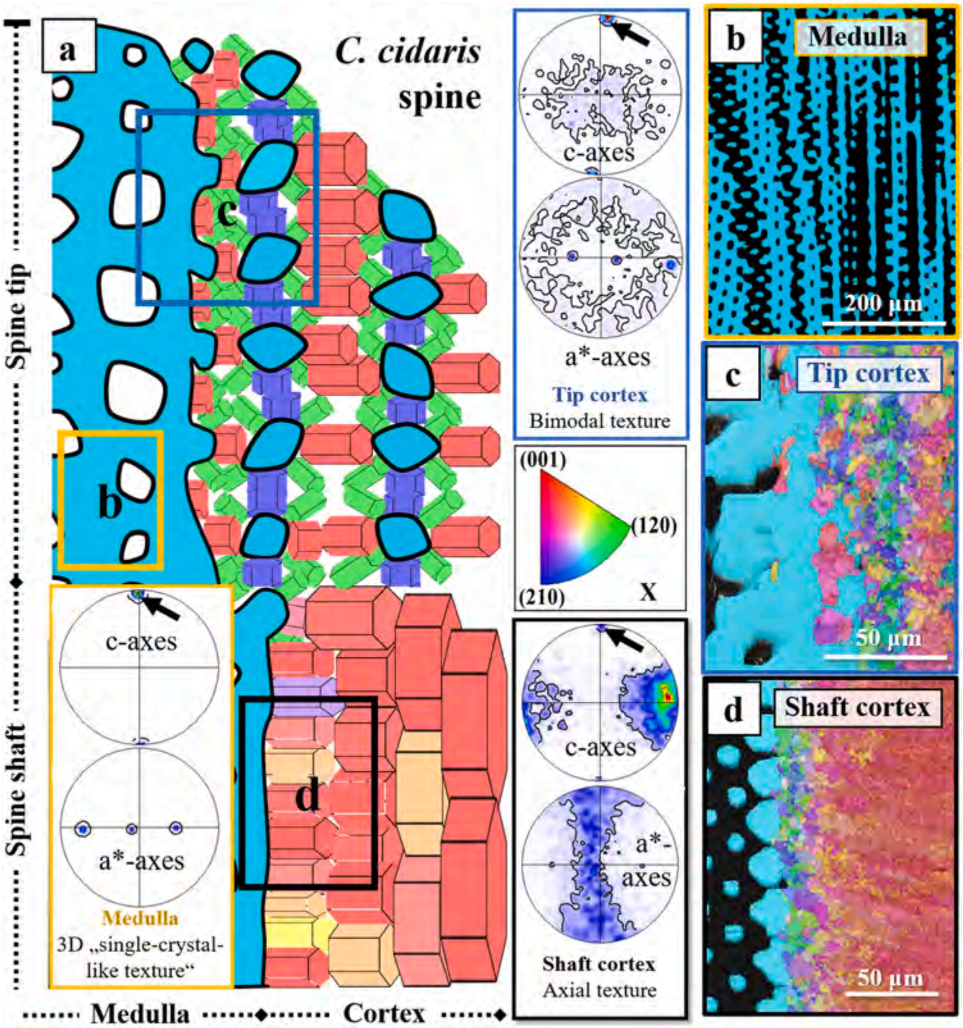

Fig. 13. Schematic illustration (a) depicting crystal arrangement of spine medulla (b), at cortex tip (c) and at cortex shaft (d) for *Cidaris cidaris*. For substantiation of the suggested crystal growth model in (a) we include the microstructure and texture of spine calcite at the medulla (b), the cortex tip (c) and the cortex shaft (d) gained from EBSD scans. Measurements were evaluated with conventional EBSD data evaluation. The sizes of the sketched hexagonal crystals in (a) illustrate the evolution of grain sizes following the competitive growth model. The shaft and tip of the spines comprise two main fabrics. The medulla is formed by highly co-oriented trabeculae organised in a galleried to rectilinear stereom (b). At growth, a series of thin parallel trabecular extensions form first. This trabecular framework functions as a substrate for the growth of the cortex crystals. At the spine tip, where a high frequency of trabecular extensions was observed, the cortex crystals spatially restrict one another in three dimensions (c). Due to the periodic arrangement of trabecular extensions, a linear pattern of small and irregular crystals becomes visible when applying an IPF colour-coded map to the measurement (c). As the series of trabecular extensions run parallel to the morphological long axis of the spine, only a small number of them perforate the shaft cortex, leaving a rather smooth nucleation template for the cortical layer (d). Thus, the crystals can competitively grow away from the medulla, generating a microstructure of increasingly large and co-oriented crystals towards the outer spine surface (d).

the spines for disclosing the degree of crystallinity of *C. cidaris* calcite. Even though this work focuses on the calcite of *C. cidaris*, we complement the obtained results on *C. cidaris* with measurements and observations on the calcite of *P. lividus* for comparison and a better understanding. With the latter, we investigate the structural hard tissue of sea urchin species of two echinoderm subclasses, the Cidaroidea and the Euechinoidea. We conclude the following for the calcitic hard tissue of *C. cidaris* and *P. lividus*.

The test:

1. Stereom trabeculae and pore arrangement in *C. cidaris* calcite develop with two main architectures. At outer test regions and surfaces, the stereom fabric is rectilinear and the pore organisation is microperforate; at inner test regions and surfaces, the stereom trabecular arrangement is labyrinthic and the pore organisation is irregular. We follow the stereom and pore nomenclature of Smith [50].
2. The test consists of calcite plates. In *C. cidaris*, these interlock intricately along the serrated edges of plates. Adjacent plates are misoriented to each other through large angle misorientations by a few tens of degrees. As EBSD data evaluation based on pattern matching demonstrates, individual test plates cannot be considered single crystals. Their calcite is rather misoriented at trabecular junctions through small-angle misorientations. Misorientations at trabecular junctions range up to 3°. Additionally, for a single crystal, MUD values should be well above 700 when calculated with a half-width of 5° and a cluster size of 3. For individual test plates, we found MUD values between 670 and 700 (half-width of 5° and cluster size 3). The decrease in MUD value for individual plates is caused mostly by low-angle misorientations at trabecular junctions. The abundance of trabecular junctions depends on the architecture of the test stereom.
3. Stereom calcite between the trabecular junctions, the intratrabecular calcite, is more or less single-crystalline. Misorientations (evaluated with EBSD pattern matching) are generally below 0.5°. MUD values are well above 700 (half-width of 5° and cluster size 3).

The tubercles:

4. The primary tubercles, the joints where the spines connect to the test plates, comprise a microstructure that differs from the stereom of the test plates. In the basal boss of the tubercle, the calcite is microperforate, formed of a dense stereom consisting of calcitic trabeculae. In the terminal knob of the tubercle, the stereom architecture is similar to that of the basal boss; however, the calcite is polycrystalline with a low crystal co-orientation strength. MUD values of the terminal knob are below 80 (half-width of 5° and cluster size 3). The basal boss is defined by a very high abundance of low-angle misorientations and, thus, a decreased MUD that scatters between 600 and 650.
5. Many crystallographic-structural aspects of tubercular calcite differ from those of the adjacent test calcite. The tubercular polycrystals have an axial texture; calcite c-axis orientations are mostly perpendicular to the outer tubercle surface. The adjacent test plates have a 3D "single-crystal-like" long-range order, with calcite c-axis orientations parallel to the surface of the test. Thus, calcite c-axis orientations of the test and of the adjacent tubercle are orthogonal.

The spines:

6. Stereom architecture, microstructure and texture of *C. cidaris* primary and secondary spines vary drastically, depending on the position within the spine. For both primary and secondary spines, we found a central galleried medulla encased by a polycrystalline cortex. For primary spines, the cortex extends over the entire shaft of the spine; for secondary spines, only about half of the spine shaft is enclosed by a cortical layer. The beginning of the cortex is determined by bumps encircling the outer surface of the medulla. For both types of spines, the cortex is thickest at the spine tip.
7. The outer surface of the medulla functions as a template for the nucleation of the cortex crystals, however, no epitaxy is evident. Along the shaft of the spine, the galleried medulla structure forms in 2D a *smooth outer surface of topologically adjacent and connected medullar galleries*. At the tip of the spine, we found a 3D, *closely-spaced network of thin galleried medullar extensions*. Cortex crystals nucleate normal to all surfaces of the outer trabeculae, with their c-axis always oriented normally to the c-axis of the medulla. Even though the outer surface of the cortex at the spine tip has a smoothness different from that of the cortex along the shaft of the spine, their growth processes are similar. The microstructure of cortex crystals is determined by growth competition.
8. The difference in cortex microstructure between the tip and the shaft of the spine is relatable to the 3D configuration of the medullar template surface (smooth or rough) and the availability of space for crystal growth. A network of round-shaped and closely-spaced medullar extensions intricately interconnected in 3D governs the tip of the spine. From the surface of these templates, crystals grow in all directions. However, due to space restrictions given by the closely-spaced medullar extensions, the growth progress is inhibited in 3D, and the 'standard competitive growth microstructure' cannot develop. We observed with the microstructure of the cortex at the very tip of the spine only the start of the competitive growth process. In contrast, along the spine shaft, towards its base, the medullar template surface is only restricted in 2D; hence, there is space for the crystals to grow away from the medulla and the competitive growth microstructure develops to advanced growth stages.
9. Since the microstructure of cortex crystals is mainly controlled by growth competition, the constitution of the medullar template and space for the growth of crystals predetermines the microstructure of cortex crystals. In contrast, the microstructure of medullar and test stereom calcite is only influenced by organism-related, biological determinants.
10. Neither *C. cidaris* nor *P. lividus* test plates, tubercles, parapets and spines should be addressed as single crystals. EBSD results show single-crystal-like, highly co-oriented sections, such as intratrabecular calcite between trabecular junctions. However, individual test plates and the medulla of the spines comprise many trabecular junctions. At all of these junctions, we observed misorientations up to 3°. Between adjacent test plates, we observed high-angle misorientations (5° to 40°). For the strongly misoriented calcite along the terminal knob and in the spines, we found also high-angle misorientations (10° to 50°).

Data availability statement

The datasets used and analysed during the current study are available from the corresponding author on reasonable request.

CRediT authorship contribution statement

Sebastian Hoerl: Writing – original draft, Visualization, Software, Methodology, Investigation. **Erika Griesshaber:** Writing – review & editing, Supervision, Software, Methodology, Investigation, Formal analysis, Data curation, Conceptualization. **Antonio G. Checa:** Writing – review & editing, Validation, Formal analysis, Data curation. **Aimo Winkelmann:** Writing – review & editing, Software, Methodology, Conceptualization. **Frank Förster:** Writing – original draft, Visualization, Investigation, Conceptualization. **Osama Alsheikha:** Visualization, Investigation. **Felix Hidalgo:** Validation, Formal analysis. **Elena Sturm:** Writing – review & editing, Formal analysis. **Sandro Jahn:** Writing – review & editing, Resources, Project administration. **Wolfgang W. Schmahl:** Writing – review & editing, Supervision, Resources, Project administration, Funding acquisition, Formal analysis.

Acknowledgements

We thank Moritz Zenkert and Verena Weideneder, Ludwig-Maximilians-Universität München, Munich, Germany, for their help with sample preparation. We thank Shahrouz Amini, Max Planck institute of Colloids and Interfaces, Potsdam, Germany, for his help with interpreting the data. W.W.S., E.G., and S.H. were funded by the German Research Council Programmes GR 9/1234, SCHM 930/11-2. A.G.C. was funded by projects PID2020-116660GB-I00 and PID2023-146394NB-I00, of the Spanish Ministerio de Ciencia e Innovación (MCIN/AEI/10.13039/501100011033/), and PCM_00092, of the Consejería de Universidad, Investigación e Innovación, Junta de Andalucía.

Supplementary materials

Supplementary material associated with this article can be found, in the online version, at doi:10.1016/j.actbio.2025.03.044.

Supplementary data associated with this manuscript can be found in the online appendix section of the manuscript.

Data availability

The authors declare that they have no known competing financial interests or personal relationships that could have appeared to influence the work reported in this paper.

References

[1] P. Domenici, D. González-Calderón, R.S. Ferrari, Locomotor performance in the sea urchin *Paracentrotus lividus*, J. Mar. Biol. Assoc. UK 83 (2003) 285–292, https://doi.org/10.1017/s0025315403007094h.

[2] R.R. Strathmann, The role of spines in preventing structural damage to echinoid tests, Paleobiology 7 (1981) 400–406.

[3] K. Simkiss, K.M. Wilbur, Biomineralization: cell biology and mineral deposition, Academic press, San Diego New York Berkeley [etc.], 1989.

[4] S.A. Wainwright, Mechanical design in organisms, Princeton University Press, 1982.

[5] W. Hasenpusch, Die Stachel der Griffelseeigel, Mikrokosmos 89 (2000) 23–27.

[6] M. Lai, A.N. Kulak, D. Law, Z. Zhang, F.C. Meldrum, D.J. Riley, Profiting from nature: macroporous copper with superior mechanical properties, Chem. Commun. (2007) 3547, https://doi.org/10.1039/b707469g.

[7] K.G. Nickel, V. Presser, S. Schultheiß, C. Berthold, C. Kohler, J. Nebelsick, N. Grossmann, T. Stegmaier, H. Finckh, A. Vohrer, Seeigelstachel als Modell für stoffdurchlässige Einschlagschutzsysteme, in: 2009: pp. 29–39.

[8] T. Yang, H. Chen, Z. Jia, Z. Deng, L. Chen, E.M. Peterman, J.C. Weaver, L. Li, A damage-tolerant, dual-scale, single-crystalline microlattice in the knobby starfish, *Protoreaster nodosus*, Science (1979) 375 (2022) 647–652, https://doi.org/10.1126/science.abj9472.

[9] T. Yang, Z. Jia, Z. Wu, H. Chen, Z. Deng, L. Chen, Y. Zhu, L. Li, High strength and damage-tolerance in echinoderm stereom as a natural bicontinuous ceramic cellular solid, Nat. Commun. 13 (2022) 6083, https://doi.org/10.1038/s41467-022-33712-z.

[10] V. Perricone, P. Cesarano, A. Mancosu, D. Asnicar, S. Bravi, F. Marmo, Echinoid skeleton: an insight on the species-specific pattern of the *Paracentrotus lividus* plate and its microstructural variability, J. R. Soc. Interface 20 (2023) 20220673, https://doi.org/10.1098/rsif.2022.0673.

[11] J.N. Weber, The incorporation of magnesium into the skeletal calcites of echinoderms, Am. J. Sci. 267 (1969) 537–566.

[12] R.Z. Wang, L. Addadi, S. Weiner, Design strategies of sea urchin teeth: structure, composition and micromechanical relations to function, Philos. Trans. R. Soc. Lond. B Biol. Sci. 352 (1997) 469–480, https://doi.org/10.1098/rstb.1997.0034.

[13] P. Dubois, L. Ameye, Regeneration of spines and pedicellariae in echinoderms: a review, Microsc. Res. Tech. 55 (2001) 427–437, https://doi.org/10.1002/jemt.1188.

[14] D.M. Raup, Ontogenetic variation in the crystallography of echinoid calcite, J. Paleontol. 34 (1960) 1041–1050.

[15] D.M. Raup, The phylogeny of calcite crystallography in echinoids, J. Paleontol. 36 (1962) 793–810.

[16] U. Magdans, H. Gies, Single crystal structure analysis of sea urchin spine calcites: Systematic investigations of the Ca/Mg distribution as a function of habitat of the sea urchin and the sample location in the spine, Eur. J. Mineral. 16 (2004) 261–268, https://doi.org/10.1127/0935-1221/2004/0016-0261.

[17] B.E. Bodenbender, Echinoderm skeletal crystallography and paleobiological applications, Paleontol. Soc. Pap. 3 (1997) 191–204, https://doi.org/10.1017/S1089332600000255.

[18] D.M. Raup, Crystallography of echinoid calcite, J. Geol. 67 (1959) 661–674.

[19] X. Su, S. Kamat, A.H. Heuer, The structure of sea urchin spines, large biogenic single crystals of calcite, J. Mater. Sci. 35 (2000) 5545–5551, https://doi.org/10.1023/A:1004840609666.

[20] G. Donnay, D.L. Pawson, X-ray diffraction studies of echinoderm plates, Science (1979) 166 (1969) 1147–1150.

[21] C. Moureaux, A. Pérez-Huerta, P. Compère, W. Zhu, T. Leloup, M. Cusack, P. Dubois, Structure, composition and mechanical relations to function in sea urchin spine, J. Struct. Biol. 170 (2010) 41–49, https://doi.org/10.1016/j.jsb.2010.01.003.

[22] H.-U. Nissen, Crystal orientation and plate structure in echinoid skeletal units, Science (1979) 166 (1969) 1150–1152, https://doi.org/10.1126/science.166.3909.1150.

[23] K. Okazaki, R.M. Dillaman, K.M. Wilbur, Crystalline axes of the spine and test of the sea urchin *Strongylocentrotus purpuratus*: Determination by crystal etching and decoration, Biol. Bull. 161 (1981) 402–415, https://doi.org/10.2307/1540945.

[24] J. Seto, Y. Ma, S.A. Davis, F. Meldrum, A. Gourrier, Y.-Y. Kim, U. Schilde, M. Sztucki, M. Burghammer, S. Maltsev, C. Jäger, H. Cölfen, Structure-property relationships of a biological mesocrystal in the adult sea urchin spine, Proc. Natl. Acad. Sci. 109 (2012) 3699–3704, https://doi.org/10.1073/pnas.1109243109.

[25] J. Aizenberg, J. Hanson, T.F. Koetzle, S. Weiner, L. Addadi, Control of macromolecule distribution within synthetic and biogenic single calcite crystals, J. Am. Chem. Soc. 119 (1997) 881–886, https://doi.org/10.1021/ja9628821.

[26] H. Cölfen, H.-B. Bürgi, D. Chernyshov, M. Stekiel, A. Chumakova, A. Bosak, B. Wehinger, B. Winkler, Mesocrystalline structure and mechanical properties of biogenic calcite from sea urchin spine, Acta Crystallogr. Sect. B Struct. Sci. Cryst. Eng. Mater. 78 (2022) 356–358, https://doi.org/10.1107/S2052520622000634.

[27] S. Zaefferer, A critical review of orientation microscopy in SEM and TEM, Cryst. Res. Technol. 46 (2011) 607–628, https://doi.org/10.1002/crat.201100125.

[28] G. Nolze, A. Winkelmann, R.S. Neumann, Significant improvement of the orientation resolution by EBSD-pattern matching, in: 2017: pp. 7–11. 10.13140/RG.2.2.17914.90564.

[29] A. Winkelmann, B.M. Jablon, V.S. Tong, C. Trager-Cowan, K.P. Mingard, Improving EBSD precision by orientation refinement with full pattern matching, J. Microsc. 277 (2020) 79–92, https://doi.org/10.1111/jmi.12870.

[30] P. Trimby, M. Al-Mosawi, M. Al-Jawad, S. Micklethwaite, Z. Aslam, A. Winkelmann, S. Piazolo, The characterisation of dental enamel using transmission Kikuchi diffraction in the scanning electron microscope combined with dynamic template matching, Ultramicroscopy 260 (2024) 113940, https://doi.org/10.1016/j.ultramic.2024.113940.

[31] W.C. Lenthe, S. Singh, M.D. Graef, A spherical harmonic transform approach to the indexing of electron back-scattered diffraction patterns, Ultramicroscopy 207 (2019) 112841, https://doi.org/10.1016/j.ultramic.2019.112841.

[32] Y. Ma, S.R. Cohen, L. Addadi, S. Weiner, Sea urchin tooth design: An "all-calcite" polycrystalline reinforced fiber composite for grinding rocks, Adv. Mater. 20 (2008) 1555–1559, https://doi.org/10.1002/adma.200702842.

[33] D. Colombera, R. Vitturi, L. Zanirato, Chromosome number of *Cidaris cidaris* (Cidaridae, Echinoidea), Acta Zool. 58 (1977) 185–186.

[34] T. Mortensen, Handbook of the echinoderms of the British Isles, Oxford university Press, London, 1927, https://doi.org/10.5962/bhl.title.6841.

[35] P.A. Tyler, J.D. Gage, The reproductive biology of echinothuriid and cidarid sea urchins from the deep sea (Rockall Trough, North-East Atlantic Ocean), Mar. Biol. 80 (1984) 63–74, https://doi.org/10.1007/BF00393129.

[36] J.M. Lawrence (Ed.), Sea urchins: biology and ecology, Academic Press, an imprint of Elsevier, London, United Kingdom ; San Diego, CA, 2020. Fourth edition.

[37] C.F. Boudouresque, M. Verlaque, *Paracentrotus lividus*. Dev. Aquac. Fish. Sci, Elsevier, 2020, pp. 447–485, https://doi.org/10.1016/B978-0-12-819570-3.00026-3.

[38] E. Hebert, M. Silvia, G.M. Wessel, Structural and molecular distinctions of primary and secondary spines in the sea urchin *Lytechinus variegatus*, Sci. Rep. 14 (2024) 28525, https://doi.org/10.1038/s41598-024-76239-7.

[39] S.E. Coppard, A. Kroh, A.B. Smith, The evolution of pedicellariae in echinoids: an arms race against pests and parasites, Acta Zool 93 (2012) 125–148, https://doi.org/10.1111/j.1463-6395.2010.00487.x.

[40] A. Battas, The symmetry and crystal arrangement of biologically formed carbonate materials, Master Thesis, Ludwig-Maximilians-Universität, 2023.

[41] E. Ballesteros, Mediterranean coralligenous assemblages: A synthesis of present knowledge, in: R.N. Gibson, R.J.A. Atkinson, J.D.M. Gordon (Eds.), Oceanogr. Mar. Biol, ed., CRC Press, 2006, pp. 135–208, https://doi.org/10.1201/9781420006391-7.

[42] A.J. Schwartz, M. Kumar, B.L. Adams, in: D.P. Field (Ed.), Electron backscatter diffraction in materials science, Springer US, Boston, MA, 2009, https://doi.org/10.1007/978-0-387-88136-2.

[43] E. Griesshaber, X. Yin, A. Ziegler, K. Kelm, A. Checa, A. Eisenhauer, W.W. Schmahl, Patterns of mineral organization in carbonate biological hard materials, in: S. Heuss-Aßbichler, G. Amthauer, M. John (Eds.), Highlights Appl. Mineral, De Gruyter, 2017, pp. 245–272, https://doi.org/10.1515/9783110497342-012.

[44] O. Engler, S. Zaefferer, V. Randle. Introduction to texture analysis: macrotexture, microtexture, and orientation mapping, 3rd ed., CRC Press, Boca Raton, 2023 https://doi.org/10.1201/9781003258339.

[45] N. Krieger Lassen, D.Juul Jensen, K. Conradsen, Image processing procedures for analysis of electron back scattering patterns, Scanning Microsc. 6 (1992) 7.

[46] S. Wright, M. Nowell, J. Basinger, Precision of EBSD based orientation measurements, Microsc. Microanal. 17 (2011) 406–407, https://doi.org/10.1017/S143192761100290X.

[47] K. Thomsen, N.H. Schmidt, A. Bewick, K. Larsen, J. Goulden, Improving the accuracy of orientation measurements using EBSD, Microsc. Microanal. 19 (2013) 724–725, https://doi.org/10.1017/S1431927613005618.

[48] A. Winkelmann, G. Nolze, G. Cios, T. Tokarski, P. Bała, Refined calibration model for improving the orientation precision of electron backscatter diffraction maps, Materials 13 (2020) 2816, https://doi.org/10.3390/ma13122816.

[49] T.A. Ebert, Growth and survival of postsettlement sea urchins, in: Dev. Aquac. Fish. Sci, Elsevier, 2007, pp. 95–134, https://doi.org/10.1016/S0167-9309(07)80070-6.

[50] A.B. Smith, Stereom microstructure of the echinoid test, Spec. Pap. Palaeontol. 25 (1980) 1–81.

[51] F. Förster, Crystallographic characterization of sea urchin skeletal elements, Master thesis, Ludwig-Maximilians-Universität, 2020.

[52] J.W. Durham, R.V. Melville, Skeletal Morphology, in: H. Exline, G. Regnéll, D.L. Pawson, C.D. Wagner, R.C. Moore, A.G. Fischer, P.M. Kier, G. Ubaghs, K.E. Caster, R.V. Kesling, D.L. Frizzell, H.B. Fell, C.W. Wright, W.K. Spencer (Eds.), Treatise Invertebr. Paleontol., Kansas, 1966. https://journals.ku.edu/InvertebratePaleo/article/view/5659 (accessed January 27, 2025).

[53] J.N. Grossmann, Stereom differentiation in sea urchin spines under special consideration as a model for a new impact protective system, Universität Tübingen, 2010.

[54] J.H. Nebelsick, J.F. Dynowski, J.N. Grossmann, C. Tötzke, Echinoderms: Hierarchically organized light weight skeletons, in: C. Hamm (Ed.), Evol. Lightweight Struct, Springer Netherlands, Dordrecht, 2015, pp. 141–155, https://doi.org/10.1007/978-94-017-9398-8_8.

[55] J.S. Pearse, V.B. Pearse, Growth zones in the echinoid skeleton, Am. Zool. 15 (1975) 731–751, https://doi.org/10.1093/icb/15.3.731.

[56] A. Dery, P.D. Tran, P. Compère, P. Dubois, Cidaroids spines facing ocean acidification, Mar. Environ. Res. 138 (2018) 9–18, https://doi.org/10.1016/j.marenvres.2018.03.012.

[57] A.B. Smith, A functional classification of the coronal pores of regular echinoids, Paleontology 21 (1978) 759–789.

[58] H.M. Ji, Q.J. Qi, S.M. Liang, H. Yu, X.W. Li, Ordered stereom structure in sea urchin tubercles: High capability for energy dissipation, Acta Biomater. 150 (2022) 310–323, https://doi.org/10.1016/j.actbio.2022.07.031.

[59] J. Grossmann, J. Nebelsick, in: C. Johnson (Ed.), Stereom differentiation in spines of *Plococidaris verticillata*, Heterocentrotus mammillatus and other regular sea urchins, Echinoderms Chang. World, Taylor & Francis Group, London, 2013, pp. 97–104.

[60] J.N. Grossmann, J.H. Nebelsick, Comparative morphological and structural analysis of selected cidaroid and camarodont sea urchin spines, Zoomorphology 132 (2013) 301–315, https://doi.org/10.1007/s00435-013-0192-5.

[61] N. Tsafnat, J.D. Fitz Gerald, H.N. Le, Z.H. Stachurski, Micromechanics of sea urchin spines, PLoS. One 7 (2012) e44140, https://doi.org/10.1371/journal.pone.0044140.

[62] J. Trotter, K. Kadler, D. Holmes, Echinoderm collagen fibrils grow by surface-nucleation-and-propagation from both centers and ends, J. Mol. Biol. 300 (2000) 531–540.

[63] K.G. Nickel, K. Klang, C. Lauer, G. Buck, Sea urchin spines as role models for biological design and integrative structures, in: S. Heuss-Aßbichler, G. Amthauer, M. John (Eds.), Highlights Appl. Mineral, De Gruyter, 2017, pp. 273–284, https://doi.org/10.1515/9783110497342-013.

[64] A. Berman, L. Addadi, Å. Kvick, L. Leiserowitz, M. Nelson, S. Weiner, Intercalation of sea urchin proteins in calcite: Study of a crystalline composite material, Science (1979) 250 (1990) 664–667, https://doi.org/10.1126/science.250.4981.664.

[65] A.G. Checa, Physical and biological determinants of the fabrication of molluscan shell microstructures, Front. Mar. Sci. 5 (2018) 353.

[66] Y.A. Shin, S. Yin, X. Li, S. Lee, S. Moon, J. Jeong, M. Kwon, S.J. Yoo, Y.-M. Kim, T. Zhang, H. Gao, S.H. Oh, Nanotwin-governed toughening mechanism in hierarchically structured biological materials, Nat. Commun. 7 (2016) 10772, https://doi.org/10.1038/ncomms10772.

[67] S. Hoerl, C. Micheletti, S. Amini, E. Griesshaber, K.-U. Hess, A.G. Checa, M. Peharda, W.W. Schmahl, Correlation between nanomechanical properties and microstructural design concepts of bivalve muscle attachment sites [submitted], Mater. Des. (2024).

[68] A. Berman, J. Hanson, L. Leiserowitz, T.F. Koetzle, S. Weiner, L. Addadi, Biological control of crystal texture: A widespread strategy for adapting crystal properties to function, Science (1979) 259 (1993) 776–779, https://doi.org/10.1126/science.259.5096.776.

[69] D.M. Raup, Crystal orientations in the echinoid apical system, J. Paleontol. 39 (1965) 934–951.

[70] D.M. Raup, Crystallographic data in echinoderm classification, Syst. Zool. 11 (1962) 97, https://doi.org/10.2307/2411872.

[71] F. Nindiyasari, A. Ziegler, E. Griesshaber, L. Fernández-Díaz, J. Huber, P. Walther, W.W. Schmahl, Effect of hydrogel matrices on calcite crystal growth morphology, aggregate formation, and co-orientation in biomimetic experiments and biomineralization environments, Cryst. Growth Des. 15 (2015) 2667–2685, https://doi.org/10.1021/cg5018483.

[72] A. Seilacher, Constructional morphology of sand dollars, Paleobiology 5 (1979) 191–221, https://doi.org/10.1017/S0094837300006527.

[73] M. Hidaka, K. Takahashi, Fine structure and mechanical properties of the catch apparatus of the sea-urchin spine, a collagenous connective tissue with muscle-like holding capacity, J. Exp. Biol. 103 (1983) 1–14, https://doi.org/10.1242/jeb.103.1.1.

[74] A.B. Smith, Biomineralization in echinoderms, in: J.G. Carter (Ed.), Skelet. Biominer. Patterns Process. Evol. Trends, Springer US, Boston, MA, 1991, https://doi.org/10.1007/978-1-4899-5391-9.

[75] K.M. Towe, Echinoderm calcite: single crystal or polycrystalline aggregate, Science (1979) 157 (1967) 1048–1050.

[76] S. Hoerl, T. Le Moine, N.J. Peter, S. Amini, E. Griesshaber, J. Wang, E.M. Harper, C. Salas, A.G. Checa, R. Schwaiger, W.W. Schmahl, Crystal organisation and material properties of *Chama* and *Glycymeris* myostraca and shells, Materialia (Oxf) 36 (2024) 102149, https://doi.org/10.1016/j.mtla.2024.102149.

[77] S. Hoerl, E. Griesshaber, A.G. Checa, W.W. Schmahl, The biological crystals in chamid bivalve shells: Diversity in morphology and crystal arrangement pattern, Crystals. (Basel) 14 (2024) 649, https://doi.org/10.3390/cryst14070649.

[78] S. Hoerl, E. Griesshaber, W.W. Schmahl, The special microstructure of the myotest in the recent brachiopod *Magellania venosa* [Manuscript in preparation], Mar. Biol. (2025).

[79] O. Alsheikha, Microstructure crystallography and chemical characterisation of synthetic and biological calcium carbonates., Master thesis, Ludwig-Maximilians-Universität, 2020.

[80] A.J. Goetz, E. Griesshaber, R. Abel, T. Fehr, B. Ruthensteiner, W.W. Schmahl, Tailored order: The mesocrystalline nature of sea urchin teeth, Acta Biomater. 10 (2014) 3885–3898, https://doi.org/10.1016/j.actbio.2014.06.012.

[81] Y. Politi, T. Arad, E. Klein, S. Weiner, L. Addadi, Sea urchin spine calcite forms via a transient amorphous calcium carbonate phase, Science (1979) 306 (2004) 1161–1164, https://doi.org/10.1126/science.1102289.

[82] A. Varkoulis, K. Voulgaris, S. Zaoutsos, A. Stratakis, D. Vafidis, Chemical composition and microstructural morphology of spines and tests of three common sea urchins species of the sublittoral zone of the Mediterranean Sea, Animals 10 (2020) 1351, https://doi.org/10.3390/ani10081351.

[83] A. Goetz, E. Griesshaber, W.W. Schmahl, An easy approach to increase the precision of EBSD analysis – Examples from a sea urchin calcite study, Solid State Phenom 160 (2010) 229–234, https://doi.org/10.4028/www.scientific.net/SSP.160.229.

[84] S.T. Hyde, F.C. Meldrum, Starfish grow extraordinary crystals, Science (1979) 375 (2022) 615–616, https://doi.org/10.1126/science.abn2717.

[85] A.-L. Jessop, A.J. Millsteed, J.J.K. Kirkensgaard, J. Shaw, P.L. Clode, G.E. Schröder-Turk, Composite material in the sea urchin *Cidaris rugosa*: ordered and disordered micrometre-scale bicontinuous geometries, J. R. Soc. Interfaces 21 (2024) 20230597, https://doi.org/10.1098/rsif.2023.0597.